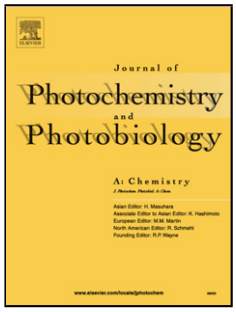

Title: Systematic variation of preparation time, temperature, and pressure in hydrothermal synthesis of macro-/mesoporous TiO_2 for photocatalytic air treatment

Authors: Alireza Haghighat Mamaghani, Fariborz Haghighat, Chang-Seo Lee

PII: S1010-6030(18)31734-9
DOI: https://doi.org/10.1016/j.jphotochem.2019.04.022
Reference: JPC 11811

To appear in: *Journal of Photochemistry and Photobiology A: Chemistry*

Received date: 27 November 2018
Revised date: 26 March 2019
Accepted date: 15 April 2019

Please cite this article as: Mamaghani AH, Haghighat F, Lee C-Seo, Systematic variation of preparation time, temperature, and pressure in hydrothermal synthesis of macro-/mesoporous TiO_2 for photocatalytic air treatment, *Journal of Photochemistry and amp; Photobiology, A: Chemistry* (2019), https://doi.org/10.1016/j.jphotochem.2019.04.022

Systematic variation of preparation time, temperature, and pressure in hydrothermal synthesis of macro-/mesoporous TiO_2 for photocatalytic air treatment

Alireza Haghighat Mamaghani, Fariborz Haghighat*, Chang-Seo Lee

Department of Building, Civil and Environmental Engineering,
Concordia University, Montreal, Canada

* Corresponding author, fariborz.haghighat@concordia.ca
E-mail addresses: alireza.haghighatmamaghani@mail.concordia.ca (A. Haghighat M), chang-seo.lee@concordia.ca (C.S. Lee)

Graphical abstract

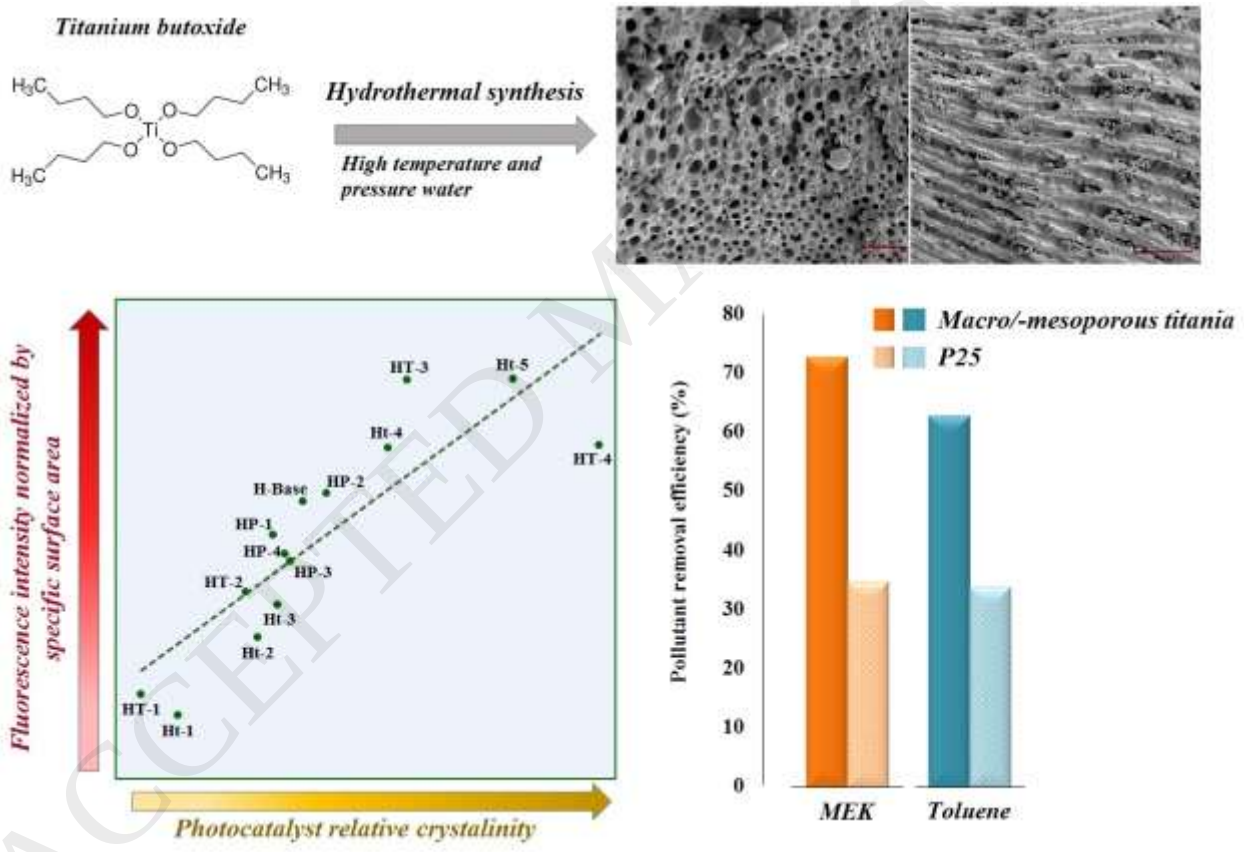

Highlights

- Macro-/mesoporous TiO_2 photocatalysts were synthesized via a hydrothermal route.
- Impacts of hydrothermal time, temperature, and pressure on titania was examined.
- $^{\bullet}OH$ generation on illuminated titania was measured by photoluminescence method.
- Correlation between crystalinity and surface area and $^{\bullet}OH$ generation was found.
- Toluene/MEK photocatalytic oxidation was conducted to evaluate activity of catalysts.

Abstract

A series of porous TiO_2 photocatalysts are prepared, by systematically varying the preparation conditions (time, temperature, or pressure (i.e. filling ratio)), characterized, and evaluated in photocatalytic oxidation of toluene and methyl ethyl ketone (MEK) to explore preparation-property-performance relationships. A detailed characterization has been conducted via X-ray diffraction (XRD), N_2 adsorption-desorption, scanning electron microscopy (SEM), transmission electron microscopy (TEM), Fourier transform infrared (FTIR), and UV-vis spectroscopy. Furthermore, hydroxyl radical ($^{\bullet}OH$) generation on the surface of TiO_2 is measured by a photoluminescence (PL) method using terephthalic acid (TA) as probe molecule. All the hydrothermally-prepared samples possessed good crystallinity (79.5-89 %), large surface area (134.9-237.2 m^2/g), small crystal size (5.9-10 nm), and mesoporous structure. SEM images revealed presence of macropores and marcochannels, and N_2 adsorption-desorption and TEM analyses indicated a significant amount of mesopores. PL and XRD results demonstrated a good proportionality between surface area normalized $^{\bullet}OH$ generation and crystallinity. The complex interplay among various properties (especially crystallinity and surface area) led to appearance of activity optimums. Photocatalyst prepared at 12 h, 200 ˚C, and 80% filling ratio exhibited the

best toluene and MEK removal efficiencies, which surpass those of P25 by factors of 2.08 and 1.85 times, respectively. The superior photocatalytic activity of developed TiO_2 catalysts might be attributed to high surface area and existence of meso-/macropores that provide a large number of active sites, and facilitate light penetration and pollutants diffusion. The presented property-activity relationships can be utilized as potential design criteria for the development of new TiO_2 photocatalysts for air purification.

Keywords: Photocatalytic oxidation (PCO); Titanium dioxide (TiO_2); Hydrothermal; Hydroxyl radical; Photoluminescence; Air purification.

1. Introduction

Since the discovery of photocatalytic splitting of water on a titanium dioxide electrode under UV light by Fujishima and Honda in 1972 [1], enormous efforts have been devoted to photocatalytic decomposition of pollutants in air and water on semiconductor photocatalysts (e.g. TiO_2, ZnO, ZrO_2, WO_3, etc) [2, 3]. Photocatalytic oxidation is a viable environmental remediation technology which has been widely investigated in recent years for indoor air purification purposes [4]. Excitation of electrons from the valence band to the conduction band by light having energy greater than semiconductor's band gap is the fundamental process in PCO. This process leads to generation of charge carriers (electron-hole pair (e^--h^+)) which react with adsorbed water, surface hydroxyl (OH) groups, and oxygen and produce reactive species such as hydroxyl radical ($^{\bullet}OH$) and superoxide radical anion ($O_2^{\bullet-}$). Chemical reactions between pollutant molecules adsorbed on the surface and active radicals decompose the challenge compound to CO_2, H_2O and light by-products [5].

Titanium dioxide is the most investigated semiconductor for both air and wastewater treatment largely owed to its strong oxidizing power, chemical stability, suitable positions of valence and conduction bands, and relatively low cost [6, 7]. TiO_2 photocatalysts could be prepared by numerous methods including sol-gel, hydrothermal, solvothermal, sonochemical, direct oxidation, microwave, microemulsion, chemical vapor deposition, and electrodeposition [8]. In the majority of synthetic methods, in the first stage high surface area and porous amorphous TiO_2 is obtained; however, the porosity and surface area are drastically diminished during the calcination at elevated temperatures because of phase transformation from amorphous to crystalline titania [9, 10]. Consequently, conventional preparation procedures that involve the calcination of amorphous titania rarely achieve large surface area, which is a critical factor in heterogeneous catalysis [11]. Accordingly, hydrothermal synthesis has been put forward as an effective route to produce titanium dioxides with high surface area and good crystallinity [12, 13]. Hydrothermal synthesis is generally defined as crystallization above the room temperature and at high pressure (> 1 atm) [14]. This method involves chemical reactions between ions or molecular species in aqueous solution and one or more solid phases [13]. Hydrothermal method offers a number of advantages: formation of anatase at relatively low temperature (< 200 ˚C), low energy consumption, defect-free nano-crystals with high specific surface area, low agglomeration between particles, and narrow particle size distribution [15, 16]. Additionally, key features of titania (e.g. crystallinity, crystal size, porosity, surface hydroxyl content, and exposed facet) can be tailored by controlling the experimental parameters including temperature, time, pressure, type of solvent, pH of solution, type of acid/base, calcination temperature, etc.

A variety of strategies have been applied to enhance the photocatalytic activity of titania: coupling TiO_2 with adsorbent materials, doping with metal/non-metal dopants, surface

modification, and constructing optimal morphological designs [15, 17, 18]. In this context, ordered macro-/mesoporous materials have attracted great attention owed to their large surface area and interconnected pore systems that allow efficient mass transfer of pollutant molecules and light penetration [19]. The most conventional technique for synthesis of these materials is templating strategy in which removable or sacrificial templates are employed to reach desired spatial arrangements [20]. However, need of expensive templates and unwanted structural changes during template removal (via calcination or dissolution) have driven scientists to develop template-free methods for production of porous nanostructures [21, 22]. Yu et al. [23] were one of the firsts who worked on the hydrothermal preparation of hierarchical titania using aqueous medium and titanium alkoxide precursor. In this study, they investigated the impact of hydrothermal time on properties and photocatalytic activity of sponge-like macro-/mesoporous titania photocatalysts towards acetone.

To date, only a few works have been done on the impact of hydrothermal synthesis parameters on titania properties and its activity for indoor air purification. Therefore, there is a lack in understanding of how catalyst features influence the pollutant removal efficiency and by-products generation. The aim of the present study is to systematically investigate the effect of preparation parameters on catalyst features and photocatalytic performance. This objective was addressed in three steps: (1) the preparation of a number of photocatalysts by varying hydrothermal time, temperature, and pressure; (2) comprehensive characterization to obtain information on key properties of titania; and (3) photoactivity assessment and highlighting the preparation-property and property-performance relationships. The variations in crystallinity, crystal size, surface area, porosity, and surface chemistry with preparation parameters were explained considering TiO_2 formation mechanism during hydrothermal synthesis. Toluene and

MEK photocatalytic degradation were selected as representatives of indoor air pollutants to evaluate the photocatalytic activity. The activity of commercial P25 (used as reference) was also assessed and compared to those of synthesized titania powders.

2. Experimental

2.1. Photocatalyst preparation

All chemicals used in this study were used as received without further purification. Distilled water was employed in the preparation of all titania samples. In a typical synthesis procedure, a calculated amount of TBOT ($Ti(OC_4H_9)_4$ from Aldrich) was added dropwise at a rate of 2 ml/min to distilled water in the absence of stirring at room temperature. The volume ratio of the reaction medium to TBOT in all experiments was fixed at 10. The solution aged for 24 h at ambient temperature (21 ˚C) and afterwards the white-yellow precipitates were filtered. The filtered solids were washed several times with distilled water until the washing solution reached pH of ca. 7, and subsequently dried at 80 ˚C for 12 h. In order to investigate the impact of reaction time, temperature, and pressure, hydrothermal reactions were conducted at different temperatures (100-220 ˚C), durations (1-48 h), and reactor filling ratios (FR, 20-90%). A specific amount of amorphous titania sample was placed in a 100 ml stainless steel autoclave with a Teflon liner and the liner was filled with distilled water until it reached the desired filling ratio. The mass ratio between the amorphous TiO_2 and water within the autoclave was kept at 0.025. The autoclave was heated at a rate of 3 ˚C/min to the target temperature, maintained at that temperature for the desired hydrothermal time, and finally cooled down (-3 ˚C/min) to room temperature. The resulting precipitate was filtered, washed with distilled water, and finally dried at 80 ˚C for 12 h as the post-synthesis thermal treatment. The hydrothermal preparation parameters as well as the assigned name to each photocatalyst are listed in Table 1.

Table 1. Hydrothermal preparation conditions of different TiO_2 photocatalysts.

2.2. Photocatalyst coating

In order to evaluate the photocatalytic performance of titania samples, titania powder was deposited on a nickel foam substrate (Shanghai Tankii Alloy Material Co). The width, height, and thickness of the filter were 10, 10, and 0.1 cm, respectively. In the first step, titania particles obtained from hydrothermal synthesis (after the final thermal treatment) were pressed to form thin pellets, which then were crushed and sieved to the size of 35-60 meshes (250-500 μm). A specific quantity of photocatalyst was added to distilled water and the mixture was stirred for 6 h at room temperature at 600 rpm to reach a homogeneous TiO_2 suspension (0.5 wt%). TiO_2 colloidal solution was coated on the Ni filter via a pipetting technique in which TiO_2 solution was placed drop by drop on the filter until the entire surface of the filter is covered with TiO_2 solution. The filter was dried at 80 ˚C for 1 h and the same coating procedure was repeated for the other side of the filter. Finally, the titania coated filter was dried overnight at 80 ˚C to remove water from the filter. The TiO_2 coated filter weight is measured and compared to that of the uncoated filter to calculate the coating density. In all experiments, the TiO_2 coating density on the substrate was kept at 1 ± 0.07 mg/cm^2. Prior to each PCO test, the TiO_2 coated filter was preheated in air oven at 80 ˚C for about 2 h to remove the physically adsorbed water vapor during storage.

2.3. Photocatalyst characterization

The crystalline structure and crystallite size were identified by X-ray diffraction (Bruker, D8 advance) with a monochromatized source of Cu-Kα radiation. The average crystal sizes of anatase, brookite, and rutile were estimated based on Scherrer formulae:

$$d_{hkl} = \frac{k\lambda}{\beta cos2\theta} \quad (1)$$

where λ is the wavelength of the Cu-Kα radiation (λ=0.15405 nm), θ the Bragg's diffraction angle, β the full width at half maximum intensity of the peak, and k a constant (0.89). For anatase, brookite, and rutile, (101), (121), and (110) peaks were respectively applied in Scherrer equation to determine the crystal size. Accordingly, the phase composition can be estimated from the integrated intensities of anatase (101), brookite (121), and rutile (110) peaks. For samples with more than one crystalline phase, the mass fractions of brookite (W_B) and rutile (W_R) were calculated according to the following equations [24]:

$$W_B = \frac{2.721A_B}{0.886A_A + 2.721A_B} \quad (2)$$

$$W_R = \frac{A_R}{0.884A_A + A_R} \quad (3)$$

where A_A, A_B, and A_R are, respectively, the integrated intensities of the anatase (101) and brookite (121), and rutile (110) peaks.

To investigate the surface morphology of TiO_2 samples scanning electron microscope (Hitachi S-4700 Model) at the acceleration voltage of 15 kV was used. Transmission electron microscopy and high-resolution transmission electron microscopy images were taken on a FEI Tecnai TF-20 S/TEM instrument. Nitrogen adsorption-desorption isotherms at liquid nitrogen temperature (77K) were measured with an AUTOSORB-1 (Quantrochrome Instruments Co.) nitrogen adsorption apparatus. The Brunauer-Emmett-Teller surface areas (S_{BET}) of the samples were evaluated by multipoint BET method using the adsorption data in the relative pressure (p/p_0) range 0.05-0.3. The pore size distributions were calculated from desorption branches of isotherms by the Density Functional Theory (DFT), assuming slit-like pores. Prior to N_2 adsorption analysis, samples were completely degassed at 120 °C for several hours (except the

sample that synthesized at 100 °C, which was degassed at 80 °C). FTIR analyses were performed using a Nicolet 6700 FT-IR spectrometer (Thermo Fisher Scientific). Spectra were collected in a range of 4000–600 cm^{-1} at a resolution of 4 cm^{-1} and an absorbance detection limit of 0.001 a.u. Air spectrum, as background, was always subtracted from the obtained FTIR spectra in all experiments. The titania samples were degassed at 80 ˚C for 12 h before performing the FTIR analysis. Photoluminescence (PL) spectra were recorded with a fluorescence spectrophotometer (Varian Cary Eclipse, Agilent). Diffuse reflectance UV-visible spectra of samples were obtained over a range of 200-800 nm by a Perkin-Elmer Lambda 750 spectrophotometer, in which $BaSO_4$ was used as the background.

2.4. Determination of hydroxyl radicals (˙OH)

In order to measure the amount of ˙OH formed on the surface of UV-illuminated TiO_2, photoluminescence method with terephthalic acid as a probe molecule was employed. It is known that hydroxyl radicals rapidly react with TA and produce highly fluorescent 2-hydroxyterephthalic acid (2-HTA) (shown in Scheme 1). Therefore, the intensity of the PL peak of 2-HTA is in proportion to the concentration of ˙OH generated on photocatalyst.

Scheme 1. Generation of 2-hydroxyterephthalic acid as a result of the reaction between terephthalic acid and hydroxyl radical.

Experimental procedures were as follows: 100 mg of TiO_2 ground powder was dispersed in 30 ml of an aqueous solution containing 2 mmol/L NaOH and 0.5 mmol/L TA in a glass dish with 9 cm diameter and 2 cm depth. The concentration of TA was chosen based on the work of Ishibashi et al. which indicated that in a solution with 10^{-3}-10^{-4} mol/L TA, the hydroxylation reactions of TA proceed mainly by •OH [25]. It has been shown that at this TA concentration, 2-HTA absorption or fluorescence quenching is not significant and the correlation between 2-HTA

concentration and PL intensity is linear [26]. The solution was stirred for 20 min in darkness at ambient temperature to obtain a homogenous suspension prior to irradiation. For illumination, a 254-nm UV lamp (Philips, TUV PL-S 5W/4P) was horizontally placed 5 cm above the center of the dish. After 15 min of illumination, 4 ml aliquot was drawn, and immediately filtered using a 0.22 µm syringe filter to remove TiO_2 particles and acquire a clear solution. The fluorescence emission intensity of 2-HTA was measured at 426 nm after excitation at 315 nm on the fluorescence spectrophotometer. The PMT voltage and width of excitation (and emission) slit were 600 V and 5 nm, respectively.

2.5. Photocatalytic activity measurement

The performances of the prepared TiO_2 samples and P25 were assessed in photocatalytic degradation of toluene and MEK in air in a single-pass continuous flow photoreactor. Fig. 1 illustrates the experimental set-up scheme used for conducting the PCO tests. The reactor is made of aluminum and has an inner cross section area of 10 cm × 10 cm and length of 130 cm. The reactor configuration allows even distributions of airflow and light irradiance on the TiO_2-coated nickel substrate. The inlet air is split into two streams: one part enters a mass flow controller (OMEGA, FMA5542-A) and the other passes through a water cylinder (i.e. humidifier) in order to keep the relative humidity level at 20 ± 3 %. The VOC pollutant (toluene or MEK) is automatically injected into the air stream by a syringe pump (KD scientific, Model KDS-210) and a 25 µL gas-tight glass-syringe (Hamilton Company). The contaminated air enters the reactor and its humidity and temperature are continuously recorded by a sensor (DATAQ instruments, Model EL-USB-2) at the reactor inlet. Two low pressure mercury UV lamps (Philips, TUV PL-S 5W/4P) with dominant wavelength of 254 nm are placed at each side of the filter, as depicted in Fig. 1. The photocatalyst is allowed to come to adsorption equilibrium with

the challenge compound before starting the PCO experiments. To do so, a dark adsorption step (i.e. lamps are off) at high concentration of the target VOC (10 ppm for toluene and 20 ppm for MEK) precedes the PCO tests. The concentration of the pollutant at downstream is monitored constantly by a PID detector (ppb3000 RAE) to detect the complete saturation of the filter by VOC. Once 100% breakthrough of the TiO_2 coated filter is seen, the injection of VOC with 1 ppm concentration is initiated and the UV lamps are switched on. In order to provide the system with sufficient time to reach steady state condition in terms of concentration, irradiance, humidity, and temperature, the reactor operates for 4 h before starting the samplings. All experiments were carried out at total light intensity (on the surface of the filter) of 5 mW/cm^2 (measured with ILT77CE Germicidal Radiometer, International light technologies). The experimental conditions at which PCO tests are performed are given in Table 2. The concentrations of toluene at the upstream and downstream are determined by gas chromatography–mass spectrometry (GC-MS). For GC-MS, air samples are taken from the reactor for 20 min using an air pump (GilAir®) with 50 ml/min airflow rate connected to an AirToxic® multi-sorbent tube (SUPELCO). Subsequently, the samples are analyzed with PerkinElmer Automated Thermal Desorber (ATD, TurboMatrix™ 650) and GC-MS (PerkinElmer Clarus® 500). For determining MEK and generated by-products concentrations, high-performance liquid chromatography (HPLC) is used. For the HPLC analysis, pollutants are absorbed on a high purity silica adsorbent coated with 2, 4-dinitrophenylhydrazine (2, 4-DNPH) cartridge (SUPLECO LpDNPH S10L, Sigma Aldrich). The sampling is performed at a rate of 1 L/min for 20 min for MEK and 1 h for by-products. The absorbed compounds are extracted from the LpDNPH cartridge with acetonitrile and elutes are analyzed by PerkinElmer Flexar HPLC

equipped with a C18 Brownlee validated micro-bore column (250 mm × 4.6 mm ID, 5 µm film thickness).

Fig. 1. Schematic presentation of the experimental set-up for PCO experiments.

Table 2. PCO tests experimental conditions (mean value ± standard deviation)

The performance of PCO system is evaluated based on the removal efficiency of VOC, PCO reaction rate, and the amount of generated by-products in the gas phase. The single-pass removal efficiency is calculated based on the amount of pollutant removed by the air filter as follows:

$$Single-pass\ removal\ efficiency, \eta\ (\%) = \frac{C_{in}^{(t)} - C_{out}^{(t)}}{C_{in}^{(t)}} \times 100 \quad (4)$$

where $C_{in}^{(t)}$ and $C_{out}^{(t)}$ are the upstream and downstream concentrations in ppb at time t (min), respectively.

The photocatalytic reaction rate over TiO_2-coated filter is determined as follows:

$$Reaction\ rate, r_{PCO} = \frac{Q_{air} \times (C_{up} - C_{down})}{m \times M_{toluene/MEK}} \times 100 \quad (5)$$

where m is the photocatalyst mass on nickel foam (g), M is toluene/MEK molecular weight (g/mol), C is the VOC concentration (g/m^3), and Q_{air} is air volumetric flow rate (m^3/min).

By-products generations during PCO reactions are found by subtracting the concentration of each compound in the upstream from that of the downstream.

$$By-products\ generation, G_i\ (ppb) = C_{i,out}^{(t)} - C_{i,in}^{(t)} \quad (6)$$

where $C_{i,in}^{(t)}$ and $C_{i,out}^{(t)}$ are the upstream and downstream concentrations of by-product i in ppb at time t (min), respectively.

3. Results and discussion

3.1. Photocatalyst characterization

3.1.1. Crystal structure

It is well-established that the crystallinity, crystal phase, and crystallite size of titanium dioxide play critical roles in photocatalytic oxidation [27, 28]. TiO_2 has three crystal phases: anatase, rutile, and brookite. Rutile is a thermodynamic stable state, while anatase and brookite are metastable state. The building block of all three crystal forms of TiO_2 is TiO_6 octahedra but with a different spatial arrangement in each phase [29]. Among these three phases, anatase is believed to be the most active polymorph of titania mainly due to its low electron-hole recombination rate [5]. XRD technique was employed to study the changes in crystallographic phases and crystal size of titania samples with hydrothermal time, temperature, and filling ratio.

Fig. 2a illustrates XRD patterns of TiO_2 samples treated for various durations at 180 ˚C and 80% filling ratio. Expectedly, the as-prepared sample (i.e. without undergoing hydrothermal treatment) is amorphous since the rate of hydrolysis reaction of titanium precursor in pure water at room temperature is low and, thus, the hydrolysis cannot proceed completely. Therefore, the TiO_2 sample before hydrothermal reactions contains a considerable amount of unhydrolyzed alkyls, which hinder crystallization by adsorbing on the surface of titania particles [30]. Contrarily, samples underwent hydrothermal treatment show presence of both anatase, as the dominant crystal phase, and brookite. After hydrothermal treatment for only 1 h, a significant phase transformation from amorphous to crystalline titania is witnessed. The diffraction peaks of Ht-1 can be indexed to anatase (JCPDS No. 21-1272) and brookite TiO_2 (JCPDS No. 29-1360). By prolonging the hydrothermal synthesis duration to 3 h, anatase and brookite peaks intensities increase, implying an improvement in crystallization. Additionally, the widths of the diffraction

peaks at 2θ=25.28 ˚ (anatase (101) plane) and 2θ=30.80 ˚ (brookite (121) plane) decrease as the hydrothermal time increases from 1 to 3 h. The sharpening of diffraction peaks stems from the increment in anatase and brookite crystal sizes from 6.1 and 7.4 nm for Ht-1 to 6.9 and 7.7 nm for Ht-2. As a consistent behavior, extending the hydrothermal synthesis time results in gradual crystal size enlargement, higher degree of crystallinity, and lower amorphous TiO_2 content (see Table 3). After 6 h of hydrothermal treatment, the TiO_2 sample contains 81.5% anatase and 18.5% brookite phase. Notably, the brookite content (mass fraction) increased with hydrothermal time up to 6 h (18.5%) and from that point on experiences a downward trend. The sample undertaken 48 h of hydrothermal treatment possesses the highest relative anatase crystallinity and largest crystal sizes due to the advancement of crystallization process with time.

The impact of hydrothermal temperature on the phase structures of titania samples is presented in Fig. 2b. With raising the hydrothermal temperature, the XRD peaks intensities significantly grow and coherently the widths of diffraction peaks of anatase and brookite become smaller. These observations support the fact that higher temperature within autoclave leads to better crystallinity (i.e. smaller amorphous content) and crystal growth. This is due to the fact that Ostwald ripening process is improved at a higher hydrothermal temperature or a longer hydrothermal time . It is known that the primary driving force for simple crystal growth is the reduction in surface energy. According to Ostwald ripening phenomenon, growth of large particles at the expense of smaller particles (and concurrent morphology evolution) is driven by the tendency to minimize the area of high surface energy faces [31]. Even at temperatures as low as 100 ˚C, crystalline titania could be synthesized, which is beneficial in terms of energy requirement and obtaining large surface areas [32]. In order to compare the crystallinity of different samples, the intensity of the (101) diffraction peak of the anatase phase was regarded as a measure. The relative crystallinity was

calculated by dividing the intensity of the (101) peak of each sample to that of H-Base. As shown in Table 3, the relative anatase crystallinity and crystal size steadily increase with hydrothermal temperature. For instance, at 100 ˚C the anatase and brookite crystal sizes are 5.9 and 7.3 nm respectively, while at 220 ˚C these values reach 9.5 and 10 nm and the relative crystallinity almost doubles. Regarding the impact of hydrothermal temperature on phase composition, there are insignificant variations in anatase content among samples prepared at temperature lower than 220 °C. The anatase content reaches its maximum at 220 °C, 89.7%, which indicates that high temperature favors anatase phase formation.

Filling ratio is defined as the volume of reaction medium to the volume of autoclave. During the hydrothermal synthesis, the pressure inside the system is the sum of the pressure generated by saturated water vapor and the pressure resulted from CO_2 evolution via decomposition of titanium precursor [33]. Accordingly, the filling ratio determines the pressure during TiO_2 crystallization. Despite its potential impact on the properties of yielded titania, this aspect of hydrothermal synthesis has rarely been discussed in previous works. Hsiao et al. [33] stated that the pressurized environment in the autoclave can improve the crystallization process. Fig. 2c depicts the XRD patterns of TiO_2 samples prepared at different autoclave filling ratios. As can be noted in Fig. 2c and Table 3, the impact of autoclave filling ratio on crystallinity and crystal size is much less in comparison to that of hydrothermal temperature or hydrothermal time. The relative crystallinity, phase composition and crystal size vary in narrow ranges by increasing the autoclave filling ratio and no consistent correlation between filling ratio and crystalline structure could be found. For example, the relative crystallinity increases by increasing the filling ratio from 20% to 40%, decreases at 60% and then increases when 80% filling ratio is applied. Evidently, simultaneous effects of pressure, temperature, and water allowed crystallization to

occur at relatively lower temperature compared to "sol-gel route + calcination" [34]. It is believed that water molecules catalyze the rearrangement of the TiO_6 octahedra in the amorphous titania by adsorption to the titania surface reaction, accelerating crystallization [35] and along with high temperature and pressure in autoclave facilitate structural changes [36].

Fig. 2. XRD patterns of photocatalysts prepared at different (a) hydrothermal durations, (b) hydrothermal temperatures, and (c) autoclave filling ratios.

Table 3. Crystalline and textural properties of titania photocatalysts prepared at various hydrothermal conditions and P25.

Scheme 2 illustrates a graphical presentation of the crystalline structure of TiO_2 before and after hydrothermal synthesis at maximum time (Ht-5), temperature (HT-4), and pressure (HP-4). The crystalline and textural properties of as-prepared titania sample (100% amorphous and 346.5 m^2/g surface area) dramatically change after the hydrothermal treatment. As can be seen, a major portion of the amorphous titania (70.7-80.7 %) transforms to crystalline anatase upon hydrothermal treatment. Compared to high hydrothermal time (48 h) or temperature (220 °C), high reactor filling ratio (i.e. pressure) leads to the formation of more brookite phase, 14.9%. The activation energy for anatase-to-brookite transformation is small (11.9 kJ/mol); while for brookite-to-rutile transformation much higher energy is required (163.8 kJ/mol) [24]. Therefore, the A→B transition can proceed at such low temperatures (100-220 °C) and results in the appearance of brookite phase after hydrothermal synthesis. Yu et al. [37] reported that the formation of brookite phase can be promoted in acidic environment. Considering that in our preparation method the reaction medium was non-acidic, it is reasonable to assume that the hydrothermal environment led to the formation of brookite phase.

Scheme 2. Graphical presentation of the impact of hydrothermal treatment on titania structure.

3.1.2. Surface area and porosity

The influence of hydrothermal preparation factors on surface area and pore structure were investigated by nitrogen adsorption-desorption technique. The BET surface area of titania samples prepared at different preparation conditions are provided in Table 3. All yielded titania samples possess high surface area, a fact which underlines the advantage of hydrothermal preparation route. The BET surface area monotonically decreases with reaction time and hydrothermal temperature which is in good agreement with the XRD results. As could also be predicted from the significant crystal growth, the surface area of the as-prepared sample decreases by 37% after 1 h of hydrothermal treatment. After this initial sharp drop, increasing the reaction time gradually diminishes the surface area until it reaches its minimum for Ht-5. Analogous to the influence of reaction time, rising the hydrothermal temperature leads to an almost linear reduction in the surface area of titania samples. As an instance, as the hydrothermal temperature is raised from 100 to 220 °C the surface area decreases from 237.2 to 139.1 m^2/g. Fig. 3 and 4 present the adsorption-desorption isotherms and the corresponding pore size distributions of as-prepared titania, Ht-1, H-Base and HT-4. Before hydrothermal treatment, the TiO_2 sample has a large surface area, 346.5 m^2/g, due to its amorphous structure. As shown in Fig. 3a, the as-prepared TiO_2 exhibits isotherm of types I and IV (BDDT classification): at low relative pressures ($p_0/p < 0.1$), the isotherm shows a high adsorption due to the presence of micropores (type I) and the narrow and continuous hysteresis loop at higher relative pressures indicates the existence of mesopores (type IV). This is also in good agreement with the pore size distribution (Fig. 4a) which confirms a huge amount of micropores (pore width < 2 nm) and smaller amount of mesopores (2 < pore width < 50 nm) in the as-prepared sample structure. All the other samples show isotherms of type IV with hysteresis loops appearing at high relative

pressures, indicating the presence of mesopores. The shapes of hysteresis loop are of type H2, associated with narrow necks and wider bodies (ink-bottle pores) . By increasing the hydrothermal time from 1 h to 12 h (Ht-1 and H-Base respectively), the hysteresis loop shifts slightly to a region with higher relative pressure, implying an increment in the average pore size. Regarding the impact of hydrothermal temperature, by rising the temperature from 180 to 220 °C (H-Base and HT-4 respectively), the hysteresis loop moves rightward and downward to a region with higher relative pressure and lower adsorbed volume, showing increment in pore size and decrement in specific surface area. All hydrothermally-prepared samples appear to possess a considerable amount of mesopores within their porous structures which could explain the high surface areas. The increment in pore sizes and the reduction in surface area at more severe hydrothermal conditions (i.e. longer time, higher temperature, and higher filling ratio) can be explained as follows. Considering the fact that smaller pores bear greater stress than the bigger ones, during hydrothermal synthesis smaller pores collapse sooner. Secondly, as evidenced by XRD analyses, at harsher hydrothermal conditions, larger crystals are formed due to the crystal growth and, thus, pores result from the aggregation of these crystals would be bigger .

Fig. 3. Nitrogen adsorption–desorption isotherms of hydrothermally-prepared titania photocatalysts; Impact of hydrothermal preparation time (a) and temperature (b).

Fig. 4. Pore-size distribution of hydrothermally-prepared titania photocatalysts; Impact of hydrothermal preparation time (a) and temperature (b).

3.1.3. SEM and TEM

The macroporous structure of the yielded titania powder was directly examined by scanning electron microscopy. The SEM images of H-Base (treated at 180 °C for 12 h and 80% filling ratio) are presented in Fig. 5. In Fig. 5a, it can be clearly seen that the yielded titania sample possesses macroporous structure with pore size ranging from 0.5-3 μm. Judging from Fig. 5b

(side view of H-Base sample), H-Base exhibits a disordered macroporous frameworks with continuous walls with thickness of about 4-8 μm extend through the whole particle. The type of reaction medium can greatly influence the pore size and shape of macroporous structure. It was proposed that when the dominant solvent in the reactor is water meso-macroporous structure with macrochannels and mesoporous walls can be expected [38]. The well-oriented macroporous channels are arranged parallel to each other and perpendicular to the outer surface of the particle. The macroporous channels formed during the hydrothermal synthesis not only can facilitate the mass transfer of pollutants molecules to the active sites of titania, but also serve as paths for emitted photons to reach the particle's interior regions. As it is shown in the inset of Fig. 5b, a portion of titania particles fused together in the form of dimers or trimmers instead of incorporating in the main structure of macro/micro porous titania. This could result from the attachment of titania particles via the condensation reaction, considering the abundance of surface OH groups on TiO2 particles. Upon the contact between TBOT droplet and water in the first step of preparation procedure, a semipermeable TiO_2 layer forms on the droplet surface. This layer divides the subsequent hydrolysis and condensation reactions. These reactions proceed inwardly, and approximately perpendicular to the external surface of the particles, as the distilled water diffuses through the outer membrane [39]. This produces microphase-separated regions of TiO_2 nanoparticles and water/alcohol channels within the TBOT droplets that undergo spontaneous radial patterning caused by the hydrodynamic flow of the solvent [40]. We suggest that the mesoporosity is partly due to the intraparticle porosity and partly due to interparticle porosity. The SEM results along with the information extracted from N_2 adsorption-desorption indicate that H-Base has a trimodal pore structure of a micro-meso-macro porous system. Moreover, the microstructure of the nickel foam filter coated with H-Base photocatalyst is

presented in Fig. 5c and d. The nickel foam filter shows a 3-D porous network with pore sizes ranging from 100 to 800 μm. As can be seen, titania nanoparticles are mostly deposited on the filter framework and in some regions particles filled the oval-shape void spaces.

Fig. 5. (a and b) SEM images of porous TiO_2 hydrothermally prepared at 180 °C and 80% filling ratio for 12 h (H-Base). (c and d) SEM images of H-Base photocatalyst coated on nickel form filter.

In order to directly study the microstructure and crystal shape, size, and phase, TEM imaging was performed. Fig. 6 illustrates TEM and HRTEM images of the sample hydrothermally treated at 180 °C and 80% filling ratio for 12 h. As can be seen in Fig 6b, the anatase and brookite crystal sizes are approximately 7.33 and 8.81 nm, respectively. The particle size distribution of the H-Base sample measured from TEM analysis is depicted in Fig. 6d. Most crystals are between 6 and 10 nm in diameter and the mean size of the counted particles is roughly 7.5 nm. These values are consistent with the crystal sizes calculated by Scherrer equation based on the XRD results for H-Base (7.6 nm for anatase and 8.3 nm for brookite). Absence of long-range ordered mesostructure in TEM images led us to believe that a part of mesoporousity was caused by the aggregation of the primary titania particles (i.e. interparticle porosity), as shown in Fig. 6b. In Fig. 6c the lattice fringes of the titania can be easily recognized which confirms high crystallinity of the sample. The lattice plane of anatase (101) with interlayer spacing of ca. 0.35 nm [16] can be observed in the HRTEM images.

Fig. 6. TEM (a) and HRTEM (b and c) images of H-Base. (d) Particle size distribution histogram of H-Base sample measured from the TEM imaging in Fig. 6a (the graph is based on the measurement of the size of 100 nanoparticles.)

3.1.4. Hydroxyl radical analysis

Photocatalyst ability to produce hydroxyl radicals has an enormous influence on the efficacy of PCO system in removal and mineralization of air contaminants. The yield of •OH radicals depends on the competition between oxidation of surface OH groups/water by holes and e^--h^+ recombination. Thus, the measurement of the formation rate of hydroxyl radicals can provide useful information to better understand the connections between catalyst features and its photocatalytic activity. Hydroxyl radical has a very short lifetime (~10^{-9} s) and high reactivity, which make it difficult to be directly measured. Consequently, a variety of indirect techniques including electron spin resonance (ESR), UV/vis absorption spectroscopy, luminescence and fluorescence have been employed [41]. In this study, the fluorescence spectrometry was applied to determine the formation rate of hydroxyl radicals on different hydrothermally-prepared samples. Fig. 7a illustrates the PL spectra of TiO_2 samples synthesized under different hydrothermal durations at 180 °C and 80% filling ratio. No PL was seen for the base solution (mixture of TA and NaOH) or the TiO_2 solution in the absence of illumination which indicates that the source of PL is 2-HTA [25]. The as-prepared amorphous titania (i.e. only underwent a drying step) shows a minimal PL intensity at 426 nm, arising from the lack of crystallinity which induces more e^--h^+ recombination and smaller number of available holes for •OH production. A steady increment in PL intensity is witnessed with prolonging the hydrothermal reaction time from 1 to 48 h which can mainly be ascribed to the enhancement in crystallinity. Regarding the impact of hydrothermal temperature, in the range of 100 to 200 °C, PL intensity exhibits an upward trend and reaches its optimum value at 200 °C. The PL intensity of HT-4 was much lower than that of HT-3 despite its superior crystallinity (see Table 3) which could probably stem from the reduction in surface area and surface hydroxyl groups population at a higher

hydrothermal reaction temperature (see FTIR spectra in section 3.1.6). In the case of autoclave filling ratio, the PL intensity does not correspond with the pressure inside the reactor, but it agrees to some extent with samples crystallinity.

Fig. 7. Variations in Photoluminescence spectra of titania photocatalysts with (a) hydrothermal duration, (b) hydrothermal temperature, and (c) autoclave filling ratio.

The relationship between the surface area normalized PL intensity (calculated based on data in Fig. 7 and Table 3) and relative anatase crystallinity is depicted in Fig. 8. Even though there are some biases in the linear correlation, a good proportionality between the two parameters can be noticed in Fig. 8. The normalized PL intensity almost linearly grows with improvement in anatase relative crystallinity. Since the PL intensity is proportional to 2-HTA concentration, which is generated by the reaction between $^{\bullet}OH$ and TA, once the contribution of surface area is removed, the quality of crystallinity mainly controls the formation rate of $^{\bullet}OH$. It is important to point out that given the high pH of solution (around 11.5) and low concentration of TA, the direct oxidation of TA by photogenerated holes is very unlikely and can be ruled out [42].

Fig. 8. Dependence of surface area normalized fluorescence intensity (a.u./(m^2/g)) on the relative anatase crystallinity of various titania photocatalysts (see Table 2).

3.1.5. UV-vis

The UV-vis absorbance spectra of titania samples with different hydrothermal synthesis conditions are illustrated in Fig. 9. As can be seen in this figure, TiO_2 only effectively absorb the UV light with wavelength shorter than 410-420 nm, which is consistent with previous studies [43]. The significant absorption around 350-400 nm can be ascribed to the excitation of electrons from the valence band to the conduction band ($O_{2p} \rightarrow Ti_{3d}$) . It is evident that all the titania samples have very similar absorption profiles (and absorption edges) in the range of 250-800 nm, indicating that their band gaps should fall within a narrow range. The band gap energies are

determined by plotting $(\alpha h\nu)^2$ versus energy of light ($h\nu$) (Tauc plot) where α is the absorption coefficient, h is the plank constant and v is the frequency. The extrapolation of the straight line from the Tauc region intercepts the x axis ($h\nu$) to give the direct band gap of the TiO_2 powder. The band gap energies of pure anatase and brookite phases are 3.23 and 3.14 eV respectively. As reported in Table 3, the band gap energies of the mixed-phase TiO_2 samples, estimated from the Tauc plot, are very close and between 3.14 and 3.23 eV depending on the phase composition.

Fig. 9. Variations in UV-vis absorbance spectra of titania photocatalysts with (a) hydrothermal duration, (b) hydrothermal temperature, and (c) autoclave filling ratio.

3.1.6. FTIR

Hydroxyl groups on TiO_2 surface can serve as active adsorption sites for pollutant molecules and, therefore their population and type can have a great impact on the photocatalytic performance. FTIR is a cheap and fast method to acquire some insights into the nature and population of surface OH groups. Fig. 10 shows the FTIR characterization of the titania samples in the OH spectral region, 3800-2600 cm^{-1}. Considering that the FTIR spectra of some of the samples are almost similar, for the sake of brevity, in Fig. 10 only some of the spectra are represented. As can be noted, the surfaces of all titania powders are abundant with OH groups, judging from the appearance of a broad and strong IR absorption in the 3600-2800 cm^{-1} range. Nonetheless, it is worth highlighting that besides surface hydroxyl groups, the absorption in this region can also result from water molecules coordinatively adsorbed on surface Ti^{4+} cation and un-dissociated water molecules attached to the surface by hydrogen bonds [44, 45]. Regarding the as-prepared sample and HT-1, several bands are observed in the 2975-2850 cm^{-1} range, which could be assigned to the C-H stretching vibration. This indicates that even after 12 h of hydrothermal treatment at 100 ˚C, still there are some unhydrolyzed butoxy groups (or other residual organic

moieties originating from the starting alkoxides) in titania structure. By comparing the broad band in the 3600-2800 cm^{-1} region in samples underwent hydrothermal reactions, it can be seen that the IR absorption gradually diminishes as the reaction time or autoclave temperature is increased. This is partly due to the fact that as the hydrothermal reactions proceed, many surface hydroxyl groups are consumed in condensation reactions to form Ti-O-Ti networks. Except the as-prepared sample, in all FTIR spectra of samples prepared at different temperatures and durations, three sharp peaks at 3693, 3670, and ~3630 cm^{-1} are detected. Generally, bands at frequencies greater than 3600 cm^{-1} are ascribed to the stretching mode of –OH species free from hydrogen bonding interactions [44, 46]. Some studies suggested that the bands at frequencies higher than 3680 cm^{-1} might belong to terminal hydroxyl groups (Ti−OH) and bands at lower frequencies can be sign of bridged −OH (Ti−OH−Ti) [45]. More specifically, the band at 3693 cm^{-1} is suggested to be a signature of isolated hydroxyl groups on titania [47]. It is interesting to note that the band at 3693 cm^{-1} has its highest intensity in the case of H-Base and HT-3. In all spectra a sharp band located at 3670 cm^{-1} can be noticed which is due to the presence of bridging −OH group [44]. Only on HT-3, a small and sharp peak appears at 3650 cm^{-1} which could be attributed to a type of isolated hydroxyl group [45]. In our previous study [48], we showed that the isolated hydroxyl groups, located at 3722-3693 cm^{-1}, have strong interaction with toluene and MEK molecules.

Fig. 10. FTIR spectra of the TiO_2 samples in the hydroxyl group region: (a) impact of hydrothermal time and (b) impact of hydrothermal temperature.

3.2. Photocatalytic activity

The photoactivity has a complex relationship with each hydrothermal synthesis parameter owed to the dependence of photocatalyst key characteristics including surface area, degree of

crystallinity, crystal size, crystal phase composition, •OH production ability, porosity, and population/type of hydroxyl groups on the preparation conditions [49]. The photocatalytic activity of yielded photocatalysts was assessed through photocatalytic oxidation of toluene and MEK in air at room temperature. For comparison, the activity of P25, which is widely recognized as a highly efficient photocatalyst under UV light, is also evaluated.

As could be easily inferred from the characterization data presented in section 3.1, hydrothermal time should have a great influence on the removal efficiency (and reaction rate) of toluene and MEK. Considering Fig. 11, the as-prepared titania sample exhibits minor toluene and MEK removal efficiencies in comparison to samples underwent hydrothermal treatment mainly due to its amorphous structure, which triggers fast e^--h^+ recombination. The sample prepared at 180 ˚C for 1 h (Ht-1) shows high toluene and MEK removal efficiencies, 41% and 34% respectively, which are higher than (for toluene) and equal to (for MEK) those of P25. The good photoactivity of Ht-1 could be mainly attributed to the formation of anatase crystals, large surface area, and mesoporous structure. After this point, VOC removal efficiency variation with hydrothermal time displays different trends depending on the challenge compound. In the case of toluene which has much weaker interaction with titania surface with respect to MEK, the significant surface area (and porosity) decrement from Ht-1 to Ht-2 overpowers the marginal enhancement in crystallinity and causes ~20% drop in the removal efficiency. This clearly indicates that the adsorption process affects the photocatalytic oxidation of toluene to a greater extent than that of MEK. By prolonging the reaction time from 3 to 12 h (i.e. Ht-2 to H-Base), toluene removal efficiency and reaction rate progressively increase and reach their optimum values, 48.7 % and 11.95×10^{-5} mol/(min.g), showing improvement over P25 with 34% removal efficiency and 8.35×10^{-5} mol/(min.g) reaction rate. Further increment in the reaction time (from 12 to 48 h)

results in a sharp decline in toluene removal efficiency, most probably due to the reduction in surface area, porosity, and surface OH density. On the other hand, MEK removal efficiency monotonically enhances with hydrothermal time, reaches its maximum value on Ht-4, and experiences a minor drop for the sample that underwent 48 h hydrothermal treatment. Besides the improvement in crystallinity which surely contributes to the upward trend of MEK removal efficiency with hydrothermal time, one should bear in mind that anatase is the most active polymorph of titania in gaseous PCO and in our experiments anatase phase content increases with the hydrothermal time (see Table 3). Notably, MEK removal efficiency and reaction rate on Ht-4 is almost two times higher than that on P25. This superiority can be attributed to Ht-4 large surface area (thrice P25), good crystallinity, proper crystal size, and high mesoporousity.

Fig. 11. Toluene and MEK removal efficiency and reaction rate for the as-prepared titania, hydrothermally-prepared TiO_2 samples synthesized at different durations (1-48 h), and P25.

As noted in Fig. 12, the trends of MEK and toluene removal efficiency (and reaction rate) with hydrothermal temperature are fairly similar. With employing a higher hydrothermal temperature, the obtained photocatalyst performs better mainly owed to the substantial enhancement in crystallinity and crystal growth (see Table 3). The observed trends indicate that the greater crystallinity at higher hydrothermal temperatures counteracted the reduction in the surface area and the net effect was positive. Many researchers proposed that the co-presence of two TiO_2 crystal phases can extend the e^--h^+ pairs lifetime and, therefore, boost the quantum efficiency. Based on the obtained results, it appears that the biphasic titania photocatalyst with 82.3% anatase and 17.7% brookite (HT-3) offers the optimum photocatalytic activity towards the selected VOCs under the employed experimental conditions. It is noteworthy that higher hydrothermal temperature can also bring about a better contact between the two crystalline phases which is crucial for a successful charge carrier transfer from one phase to another.

Another possible explanation for achieving the highest photocatalytic activity over HT-3 could be its crystal size, considering that the charge carrier recombination can take place both in the bulk and on the surface of TiO_2. It is known that with crystal growth the bulk recombination becomes more significant; consequently, one can envisage a crystal size at which the best trade-off between surface and bulk recombinations exists. The fluorescence spectrometry data can be useful to better justify this point since photocatalyst capability to produce $^{\bullet}OH$ is closely connected to the population of available holes, which in turn is a measure of the effectiveness of charge carrier separation. As can be seen in Fig. 7b, HT-3 possesses the largest PL intensity amongst samples treated at different hydrothermal temperatures which might be partly ascribed to its ideal crystal size that enhances the e^--h^+ separation and subsequently the removal of challenge compounds. Additionally, although the removal efficiency does not always match the population of hydroxyl groups on titania surface in our study, as showed in Fig. 10b, the IR absorbance for HT-3 in the OH spectral region is stronger than that for HT-4. As mentioned before, surface OH groups are extremely important adsorption centers for VOC molecules. MEK can be adsorbed on the surface via H-bonding between its carbonyl group and surface OH groups, and toluene adsorption mainly occurs through weak Π-bonding to surface hydroxyls [48]. Therefore, the lower concentration of OH groups along with the smaller surface area and porosity can explain the inferior photocatalytic performance of HT-4 with respect to HT-3.

Fig. 12. Toluene and MEK removal efficiency and reaction rate for hydrothermally-prepared TiO_2 samples synthesized at different hydrothermal temperatures (100-220 °C).

Fig. 13 illustrates toluene and MEK removal efficiencies (and reaction rate) for titania powders synthesized at 180 °C for 12h with different reactor filling ratios. Evidently, the removal efficiencies cannot be correlated with the applied filling ratio which is reasonable taking into account that the variations in photocatalysts characteristics with this preparation parameter were

unpredictable as well (see Table 3). Nonetheless, it is worth highlighting that the impact of autoclave filling ratio on toluene and MEK photocatalytic oxidation is much less with respect to that of the other preparation parameters, namely hydrothermal temperature and time. Considering Fig. 13, H-Base (180 °C, 12h, and 80%) indicates the highest removal efficiency for both toluene and MEK which is in good agreement with the results reported in Fig. 7c on the PL intensity of these samples. On the other hand, although HP-3 has comparable surface area and crystallinity to those of other HP samples, it has the lowest toluene removal efficiency (31.4%) and the third lowest MEK removal efficiency (29%), which could result from its poor ability to produce hydroxyl radicals as can be evidenced in Fig. 7c.

Fig. 13. Toluene and MEK removal efficiency and reaction rate for hydrothermally-prepared TiO_2 samples synthesized at different autoclave filling ratios (20-90%).

Table 4 summarizes the amounts of detected by-products in the gas phase during the PCO of toluene and MEK on various titania samples. By comparing the data in Table 4 and Figs. 11-13, it can be noted that though many of the samples outperformed P25 in MEK/toluene degradation, the amounts of by-products in the outlet stream are considerably larger for P25. This observation can be described from two perspectives: (i) the complete conversion of challenge compounds to CO_2 and H_2O is greater on the hydrothermally prepared samples or (ii) generated by-products during PCO reactions are more efficiently adsorbed on the prepared samples compared to P25. Both views can be explained by considering the larger surface area of hydrothermally prepared samples, which provide a larger number of accessible active sites for chemical reactions (i.e. more complete mineralization) and more adsorption sites for by-products (i.e. less adsorption competition). Additionally, the porous structure of fabricated titania photocatalysts can retard the desorption of by-products (or intermediates) from the surface to the gas phase and, thus, boost the possibility of participation in further oxidation reactions [50]. In some of the PCO

experiments, propionaldehyde is found in the outlet air, while in other cases formaldehyde, acetaldehyde and acetone are the only by-products. One reason might be the low concentration of propionaldehyde which was lower than the detection limit of the HPLC. Regardless of the photocatalyst and the achieved efficiency, as a consistent trend, more by-products are generated during MEK degradation compared to that of toluene which agrees with previous works on toluene and MEK photocatalytic oxidation studies [51]. This might be attributed to the severe adsorption competition between MEK and generated by-products during its oxidation and/or the strong adsorption of toluene by-products (e.g. benzoic acid and benzaldehyde) on titania.

Table 4. Generated by-products in the gas phase during photocatalytic degradation of toluene and MEK on various titania photocatalysts (all values in ppb).

In this study, crystallinity, crystal size, phase composition, surface area, porosity, surface OH density, and $^{\bullet}$OH generation ability are the main factors. On the one hand, these parameters are interconnected and can negatively/positively (and to different magnitudes) affect photocatalytic processes. On the other hand, similar to many examples in the field of catalysis, there are thresholds for photocatalyst properties, at which sharp changes in the activity are seen due to a small variation in a property. For instance, in terms of relative crystallinity, surface area, band gap, $^{\bullet}$OH generation and crystal size, there are very small differences between Ht-3 and HP-1 (see Table 3 and Fig. 7). These samples mainly differ from each other in the anatase content, 81.5 vs 83.7%. Evidently, this slight difference in phase composition could lead to 12% difference in MEK removal efficiency (see Figs. 11 and 13). The above-mentioned issues along with the non-linear correlation between each photocatalyst feature and its activity could account for the absence of any mechanistic property-performance relationships. Nevertheless, as can be noted in Fig. 14 in the majority of cases, there is an acceptable level of proportionality between MEK/toluene removal efficiency and PL intensity. Especially for MEK photocatalytic

degradation, removal efficiencies over Ht-series and HT-series photocatalysts correspond very well with their PL intensities (coefficient of determination (R^2)=0.82). The positive correlations in Fig. 14 point out that generally higher PL intensity (or •OH generation efficiency) brings about better VOC removal efficiencies.

Fig. 14. Dependence of toluene (A) and MEK (B) removal efficiency on PL intensity.

Conclusion

In the present work, biphasic macro-/mesoporous TiO_2 photocatalysts with high specific surface area and good crystallinity were fabricated by a facile and straightforward hydrothermal route. The characterization results indicated that the hydrothermal time and temperature have significant impacts on the physical properties of prepared samples, while autoclave filling ratio is comparatively less influential. With prolonging the hydrothermal reactions or raising the hydrothermal temperature, crystallinity, crystal size, anatase phase content, and pore size increased while specific surface area, porosity, and hydroxyl groups population declined. Based on the N_2 adsorption-desorption isotherms, and SEM and TEM images, hydrothermally-prepared sample at 180 °C, 12 h, and 80% filling percentage possessed a trimodal porous structure: macroporous channels, inter- and intraparticle mesoporousity, and small amount of microporousity. The •OH generation on TiO_2 samples was assessed by photoluminescence method using terephthalic acid as probe compound. The fluorescence intensity normalized by the sample surface area could be satisfactorily correlated with the relative anatase crystallinity, indicating that the level of crystallinity mainly governs the formation rate of •OH. Generally, VOC removal efficiency improved with increasing the hydrothermal time/temperature, reached an optimum value, and then experienced a decrement due to substantial surface area and porosity loss. Toluene removal efficiency over H-Base (48.7%) and HT-3 (63%), and MEK removal

efficiency over Ht-4 (68%) and HT-3 (73%) exceeded those of P25 (34 and 35%, respectively), which could be mainly attributed to the large surface area, good crystallinity, proper crystal size, high mesoporousity, and abundance of surface hydroxyl groups of these photocatalysts. A relatively good correlation (R^2=0.66-0.82) between VOC removal efficiency and PL intensity was noticed for the majority of photocatalysts. This shows that the photoluminescence spectroscopy can be applied as a reliable and fast strategy to have a preliminary evaluation of photocatalyst performance for air purification.

Acknowledgement

The authors would like to express their gratitude to Concordia University for the support through the Concordia Research Chair – Energy & Environment.

References

[1] A. Fujishima, K. Honda, Electrochemical Photolysis of Water at a Semiconductor Electrode, Nature, 238 (1972) 37.
[2] A. Di Paola, E. García-López, G. Marcì, L. Palmisano, A survey of photocatalytic materials for environmental remediation, Journal of Hazardous Materials, 211-212 (2012) 3-29.
[3] C. Yu, W. Zhou, H. Liu, Y. Liu, D.D. Dionysiou, Design and fabrication of microsphere photocatalysts for environmental purification and energy conversion, Chemical Engineering Journal, 287 (2016) 117-129.
[4] R.A.R. Monteiro, A.M.T. Silva, J.R.M. Ângelo, G.V. Silva, A.M. Mendes, R.A.R. Boaventura, V.J.P. Vilar, Photocatalytic oxidation of gaseous perchloroethylene over TiO2 based paint, Journal of Photochemistry and Photobiology A: Chemistry, 311 (2015) 41-52.
[5] A.H. Mamaghani, F. Haghighat, C.-S. Lee, Photocatalytic oxidation technology for indoor environment air purification: The state-of-the-art, Applied Catalysis B: Environmental, 203 (2017) 247-269.
[6] A.H. Mamaghani, F. Haghighat, C.-S. Lee, Photocatalytic degradation of VOCs on various commercial titanium dioxides: Impact of operating parameters on removal efficiency and by-products generation, Building and Environment, 138 (2018) 275-282.
[7] M. Sboui, S. Bouattour, L.F. Liotta, V.L. Parola, M. Gruttadauria, G. Marcì, S. Boufi, Paper-TiO2 composite: An effective photocatalyst for 2-propanol degradation in gas phase, Journal of Photochemistry and Photobiology A: Chemistry, 350 (2018) 142-151.
[8] X. Chen, S.S. Mao, Titanium Dioxide Nanomaterials: Synthesis, Properties, Modifications, and Applications, Chemical Reviews, 107 (2007) 2891-2959.

[9] M. Ouzzine, M.A. Lillo-Ródenas, A. Linares-Solano, Photocatalytic oxidation of propene in gas phase at low concentration by optimized TiO2 nanoparticles, Applied Catalysis B: Environmental, 134-135 (2013) 333-343.
[10] A. Bazyari, A.A. Khodadadi, A. Haghighat Mamaghani, J. Beheshtian, L.T. Thompson, Y. Mortazavi, Microporous titania–silica nanocomposite catalyst-adsorbent for ultra-deep oxidative desulfurization, Applied Catalysis B: Environmental, 180 (2016) 65-77.
[11] A. Alonso-Tellez, R. Masson, D. Robert, N. Keller, V. Keller, Comparison of Hombikat UV100 and P25 TiO2 performance in gas-phase photocatalytic oxidation reactions, Journal of Photochemistry and Photobiology A: Chemistry, 250 (2012) 58-65.
[12] Y. Zhu, T. Mei, Y. Wang, Y. Qian, Formation and morphology control of nanoparticlesvia solution routes in an autoclave, Journal of Materials Chemistry, 21 (2011) 11457-11463.
[13] K. Byrappa, T. Adschiri, Hydrothermal technology for nanotechnology, Progress in Crystal Growth and Characterization of Materials, 53 (2007) 117-166.
[14] A.H. Mamaghani, F. Haghighat, C.-S. Lee, Hydrothermal/solvothermal synthesis and treatment of TiO2 for photocatalytic degradation of air pollutants: Preparation, characterization, properties, and performance, Chemosphere, 219 (2019) 804-825.
[15] E. Grabowska, M. Marchelek, T. Klimczuk, G. Trykowski, A. Zaleska-Medynska, Noble metal modified TiO2 microspheres: Surface properties and photocatalytic activity under UV–vis and visible light, Journal of Molecular Catalysis A: Chemical, 423 (2016) 191-206.
[16] Z. Wu, Z. Gu, W. Zhao, H. Wang, Photocatalytic oxidation of gaseous benzene over nanosized TiO2 prepared by solvothermal method, Chinese Science Bulletin, 52 (2007) 3061-3067.
[17] M.-V. Sofianou, C. Trapalis, V. Psycharis, N. Boukos, T. Vaimakis, J. Yu, W. Wang, Study of TiO2 anatase nano and microstructures with dominant {001} facets for NO oxidation, Environmental Science and Pollution Research, 19 (2012) 3719-3726.
[18] R. Shahbazi, A. Payan, M. Fattahi, Preparation, evaluations and operating conditions optimization of nano TiO2 over graphene based materials as the photocatalyst for degradation of phenol, Journal of Photochemistry and Photobiology A: Chemistry, 364 (2018) 564-576.
[19] R. Wang, X. Cai, F. Shen, Preparation of TiO2 hollow microspheres by a novel vesicle template method and their enhanced photocatalytic properties, Ceramics International, 39 (2013) 9465-9470.
[20] X. Li, J. Yu, M. Jaroniec, Hierarchical photocatalysts, Chemical Society Reviews, 45 (2016) 2603-2636.
[21] A. Collins, D. Carriazo, S.A. Davis, S. Mann, Spontaneous template-free assembly of ordered macroporous titania, Chemical Communications, (2004) 568-569.
[22] Q. Zhang, W. Wang, J. Goebl, Y. Yin, Self-templated synthesis of hollow nanostructures, Nano Today, 4 (2009) 494-507.
[23] J. Yu, L. Zhang, B. Cheng, Y. Su, Hydrothermal Preparation and Photocatalytic Activity of Hierarchically Sponge-like Macro-/Mesoporous Titania, The Journal of Physical Chemistry C, 111 (2007) 10582-10589.
[24] H. Zhang, J.F. Banfield, Understanding Polymorphic Phase Transformation Behavior during Growth of Nanocrystalline Aggregates: Insights from TiO2, The Journal of Physical Chemistry B, 104 (2000) 3481-3487.
[25] K.-i. Ishibashi, A. Fujishima, T. Watanabe, K. Hashimoto, Detection of active oxidative species in TiO2 photocatalysis using the fluorescence technique, Electrochemistry Communications, 2 (2000) 207-210.

[26] E. Jimenez-Relinque, M. Castellote, Quantification of hydroxyl radicals on cementitious materials by fluorescence spectrophotometry as a method to assess the photocatalytic activity, Cement and Concrete Research, 74 (2015) 108-115.
[27] R.M. Mohamed, A.A. Ismail, M.W. Kadi, D.W. Bahnemann, A comparative study on mesoporous and commercial TiO2 photocatalysts for photodegradation of organic pollutants, Journal of Photochemistry and Photobiology A: Chemistry, 367 (2018) 66-73.
[28] M. Bellardita, A. Di Paola, B. Megna, L. Palmisano, Determination of the crystallinity of TiO2 photocatalysts, Journal of Photochemistry and Photobiology A: Chemistry, 367 (2018) 312-320.
[29] N.M. Kinsinger, A. Wong, D. Li, F. Villalobos, D. Kisailus, Nucleation and Crystal Growth of Nanocrystalline Anatase and Rutile Phase TiO2 from a Water-Soluble Precursor, Crystal Growth & Design, 10 (2010) 5254-5261.
[30] J. Yu, J.C. Yu, W. Ho, M.K.P. Leung, B. Cheng, G. Zhang, X. Zhao, Effects of alcohol content and calcination temperature on the textural properties of bimodally mesoporous titania, Applied Catalysis A: General, 255 (2003) 309-320.
[31] R.L. Penn, J.F. Banfield, Morphology development and crystal growth in nanocrystalline aggregates under hydrothermal conditions: insights from titania, Geochimica et Cosmochimica Acta, 63 (1999) 1549-1557.
[32] R.K. Wahi, Y. Liu, J.C. Falkner, V.L. Colvin, Solvothermal synthesis and characterization of anatase TiO2 nanocrystals with ultrahigh surface area, Journal of Colloid and Interface Science, 302 (2006) 530-536.
[33] P.-T. Hsiao, M.-D. Lu, Y.-L. Tung, H. Teng, Influence of Hydrothermal Pressure during Crystallization on the Structure and Electron-Conveying Ability of TiO2 Colloids for Dye-Sensitized Solar Cells, The Journal of Physical Chemistry C, 114 (2010) 15625-15632.
[34] J. Ovenstone, Preparation of novel titania photocatalysts with high activity, Journal of Materials Science, 36 (2001) 1325-1329.
[35] K. Yanagisawa, J. Ovenstone, Crystallization of Anatase from Amorphous Titania Using the Hydrothermal Technique: Effects of Starting Material and Temperature, The Journal of Physical Chemistry B, 103 (1999) 7781-7787.
[36] G. Li, S. Ciston, Z.V. Saponjic, L. Chen, N.M. Dimitrijevic, T. Rajh, K.A. Gray, Synthesizing mixed-phase TiO2 nanocomposites using a hydrothermal method for photo-oxidation and photoreduction applications, Journal of Catalysis, 253 (2008) 105-110.
[37] J. Yu, Y. Su, B. Cheng, M. Zhou, Effects of pH on the microstructures and photocatalytic activity of mesoporous nanocrystalline titania powders prepared via hydrothermal method, Journal of Molecular Catalysis A: Chemical, 258 (2006) 104-112.
[38] J.L. Blin, A. Léonard, Z.Y. Yuan, L. Gigot, A. Vantomme, A.K. Cheetham, B.L. Su, Hierarchically Mesoporous/Macroporous Metal Oxides Templated from Polyethylene Oxide Surfactant Assemblies, Angewandte Chemie International Edition, 42 (2003) 2872-2875.
[39] Y.J. G., S.Y. R., C. B., Template-Free Fabrication and Enhanced Photocatalytic Activity of Hierarchical Macro-/Mesoporous Titania, Advanced Functional Materials, 17 (2007) 1984-1990.
[40] A. Vantomme, A. Léonard, Z.-Y. Yuan, B.-L. Su, Self-formation of hierarchical micro-meso-macroporous structures: Generation of the new concept “Hierarchical Catalysis”, Colloids and Surfaces A: Physicochemical and Engineering Aspects, 300 (2007) 70-78.
[41] G. Bartosz, Use of spectroscopic probes for detection of reactive oxygen species, Clinica Chimica Acta, 368 (2006) 53-76.

[42] T. Hirakawa, Y. Nosaka, Properties of O2•- and OH• Formed in TiO2 Aqueous Suspensions by Photocatalytic Reaction and the Influence of H2O2 and Some Ions, Langmuir, 18 (2002) 3247-3254.
[43] W.-K. Jo, H.-J. Kang, (Ratios: 5, 10, 50, 100, and 200) Polyaniline–TiO2 composites under visible- or UV-light irradiation for decomposition of organic vapors, Materials Chemistry and Physics, 143 (2013) 247-255.
[44] C.L. Bianchi, S. Gatto, C. Pirola, A. Naldoni, A. Di Michele, G. Cerrato, V. Crocellà, V. Capucci, Photocatalytic degradation of acetone, acetaldehyde and toluene in gas-phase: Comparison between nano and micro-sized TiO2, Applied Catalysis B: Environmental, 146 (2014) 123-130.
[45] H. Lin, J. Long, Q. Gu, W. Zhang, R. Ruan, Z. Li, X. Wang, In situ IR study of surface hydroxyl species of dehydrated TiO2: towards understanding pivotal surface processes of TiO2 photocatalytic oxidation of toluene, Physical Chemistry Chemical Physics, 14 (2012) 9468-9474.
[46] J. Araña, J.M. Doña-Rodríguez, O. González-Díaz, E. Tello Rendón, J.A. Herrera Melián, G. Colón, J.A. Navío, J. Pérez Peña, Gas-phase ethanol photocatalytic degradation study with TiO2 doped with Fe, Pd and Cu, Journal of Molecular Catalysis A: Chemical, 215 (2004) 153-160.
[47] J. Araña, A.P. Alonso, J.M.D. Rodríguez, G. Colón, J.A. Navío, J.P. Peña, FTIR study of photocatalytic degradation of 2-propanol in gas phase with different TiO2 catalysts, Applied Catalysis B: Environmental, 89 (2009) 204-213.
[48] A.H. Mamaghani, F. Haghighat, C.-S. Lee, Gas phase adsorption of volatile organic compounds onto titanium dioxide photocatalysts, Chemical Engineering Journal, 337 (2018) 60-73.
[49] A.H. Mamaghani, H. Fariborz, L. Chang-Seo, Photocatalytic oxidation of MEK over hierarchical TiO2 catalysts: Effect of photocatalyst features and operating conditions, Applied Catalysis B: Environmental, (2019).
[50] A. Haghighatmamaghani, F. Haghighat, C.-S. Lee, Performance of various commercial TiO2 in photocatalytic degradation of a mixture of indoor air pollutants: Effect of photocatalyst and operating parameters, Science and Technology for the Built Environment, (2018) 1-15.
[51] L. Zhong, F. Haghighat, C.-S. Lee, N. Lakdawala, Performance of ultraviolet photocatalytic oxidation for indoor air applications: Systematic experimental evaluation, Journal of Hazardous Materials, 261 (2013) 130-138.

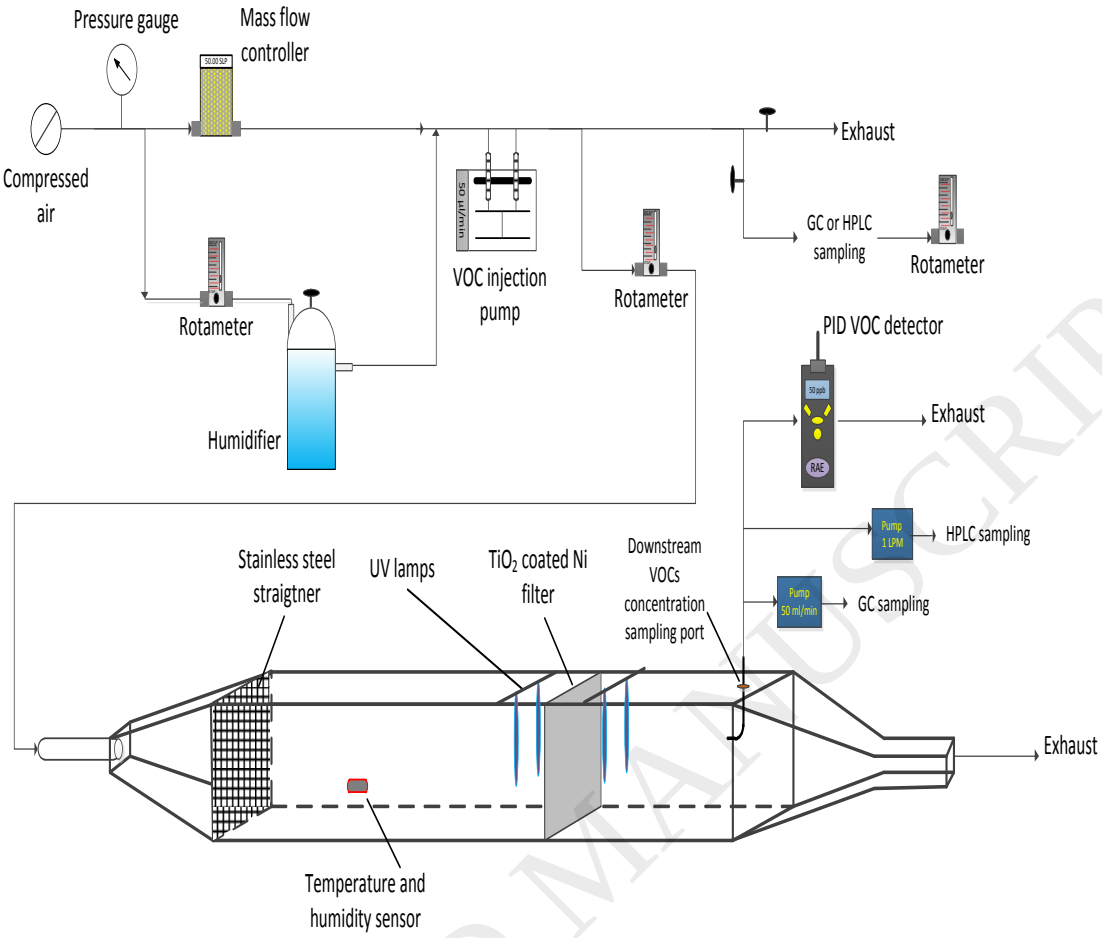

Fig. 1. Schematic presentation of the experimental set-up for PCO experiments.

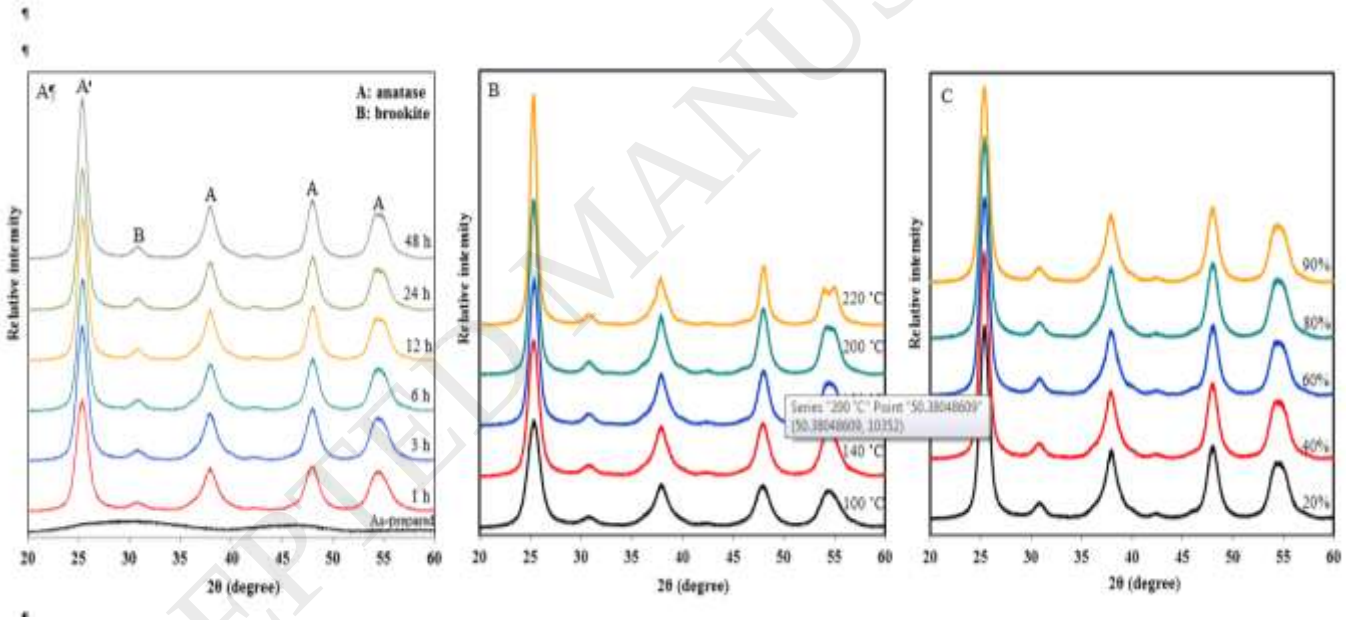

Fig. 2. XRD patterns of photocatalysts prepared at different (a) hydrothermal durations, (b) hydrothermal temperatures, and (c) autoclave filling ratios.

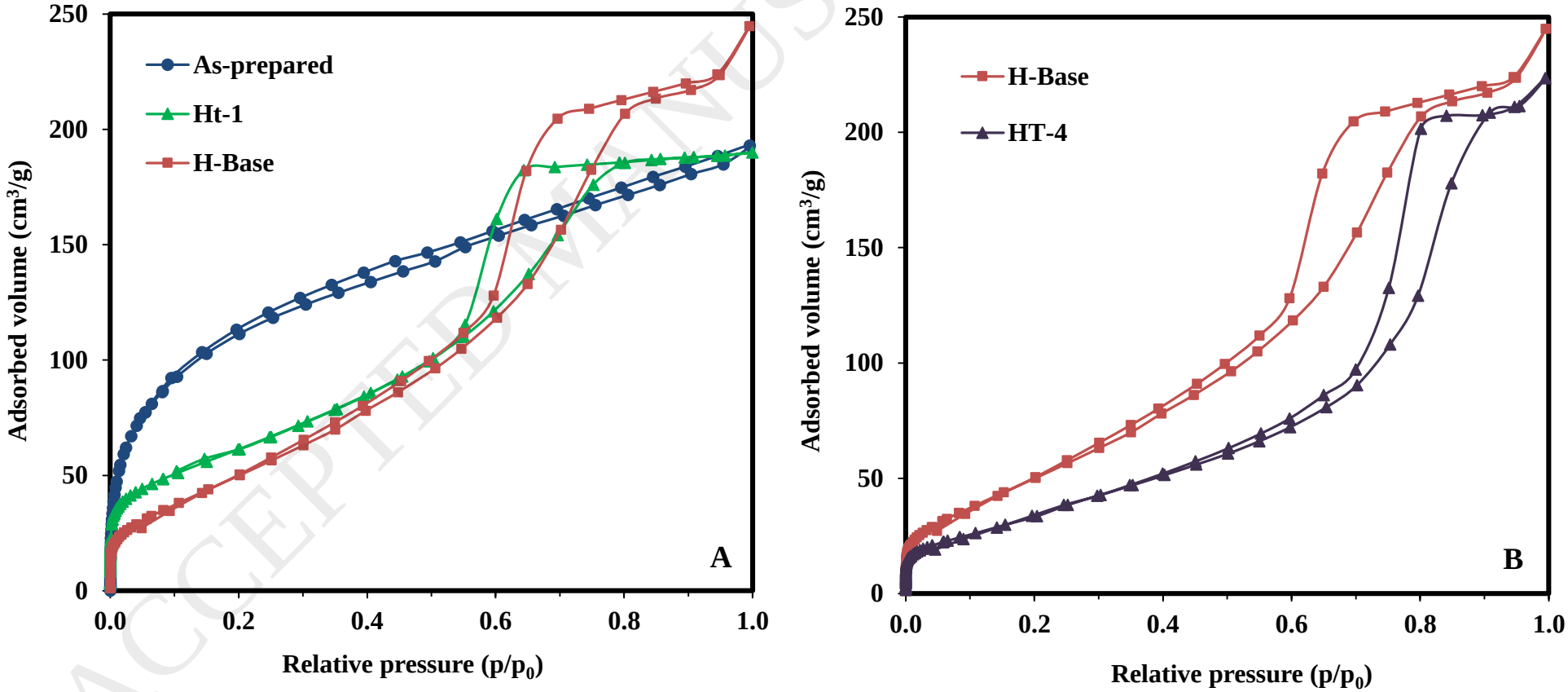

Fig. 3. Nitrogen adsorption–desorption isotherms of hydrothermally-prepared titania photocatalysts; Impact of hydrothermal preparation time (a) and temperature (b).

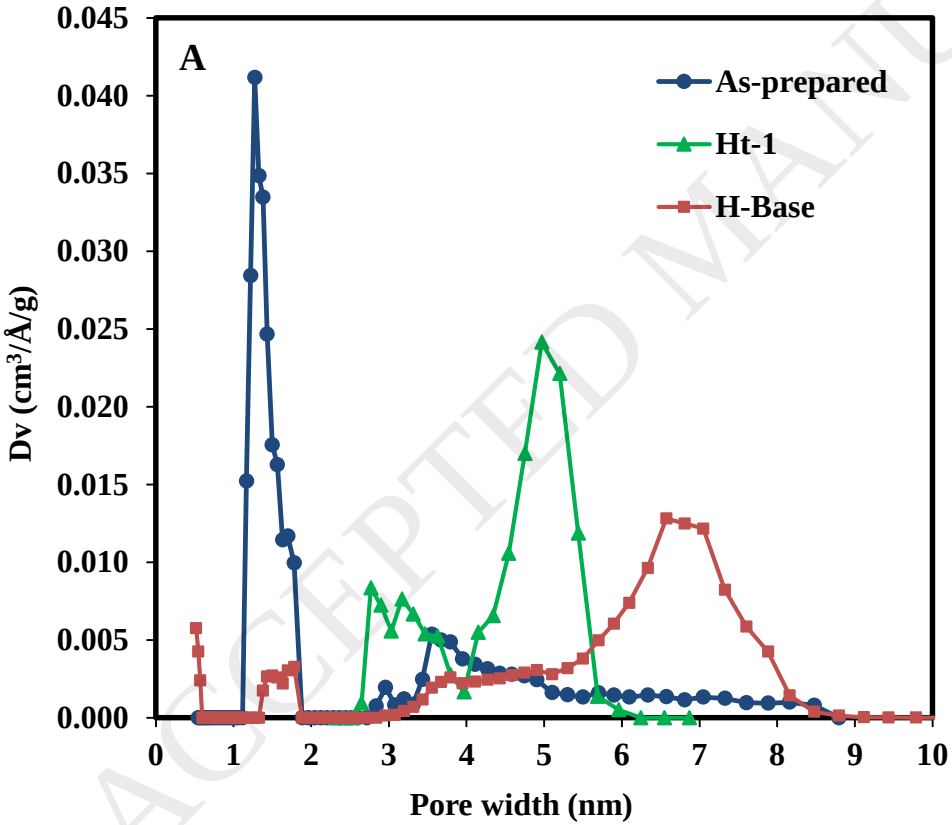

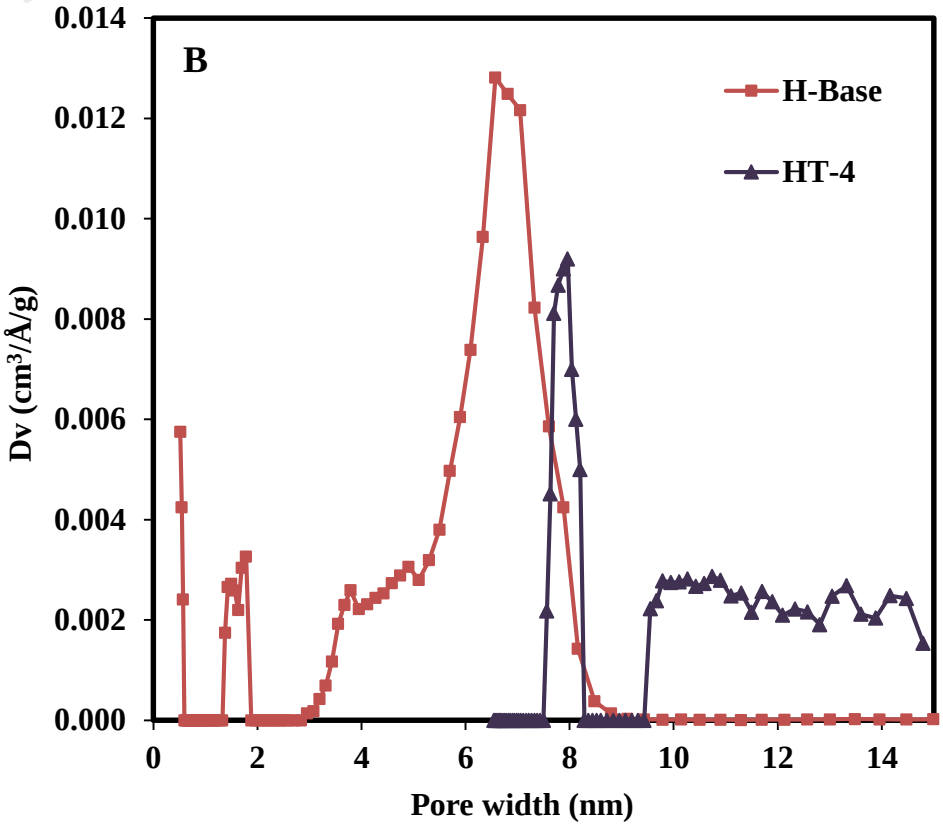

Fig. 4. Pore-size distribution of hydrothermally-prepared titania photocatalysts; Impact of hydrothermal preparation time (a) and temperature (b).

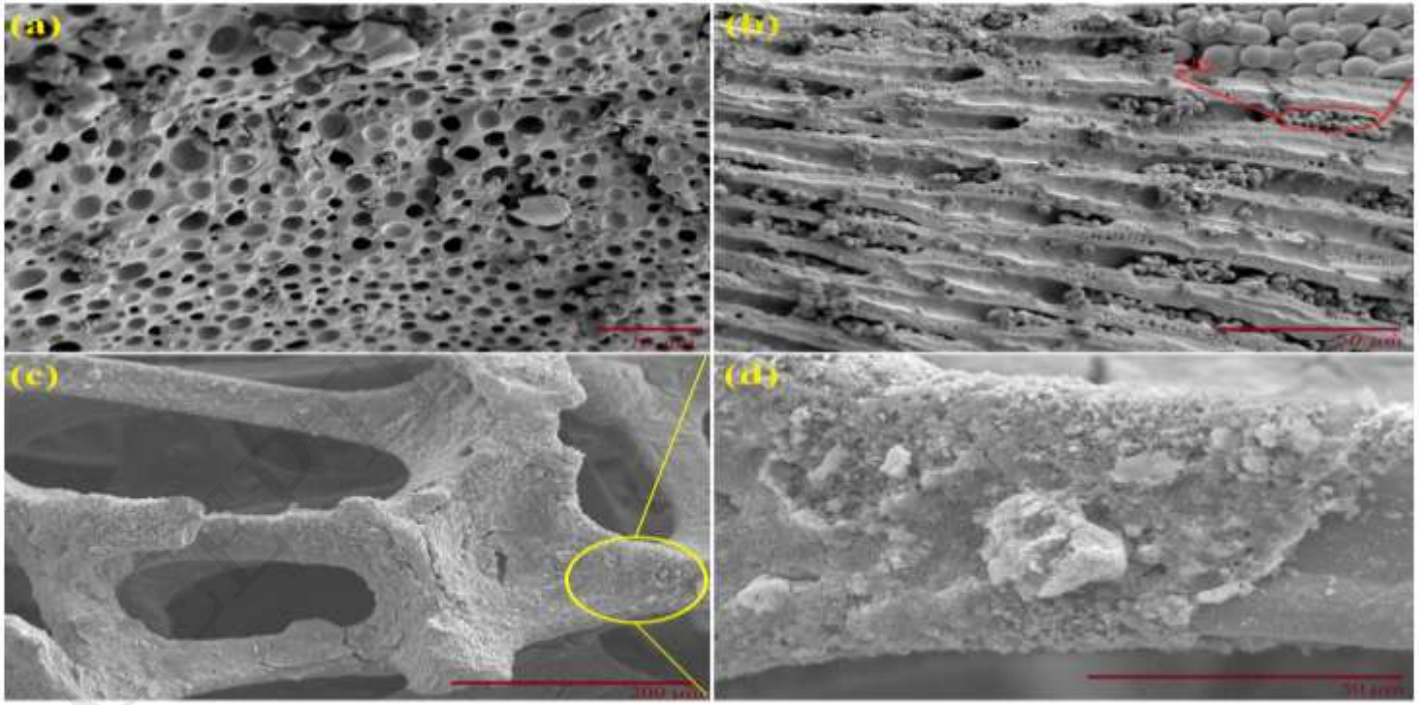

Fig. 5. (a and b) SEM images of porous TiO_2 hydrothermally prepared at 180 °C and 80% filling ratio for 12 h (H-Base). (c and d) SEM images of H-Base photocatalyst coated on nickel form filter.

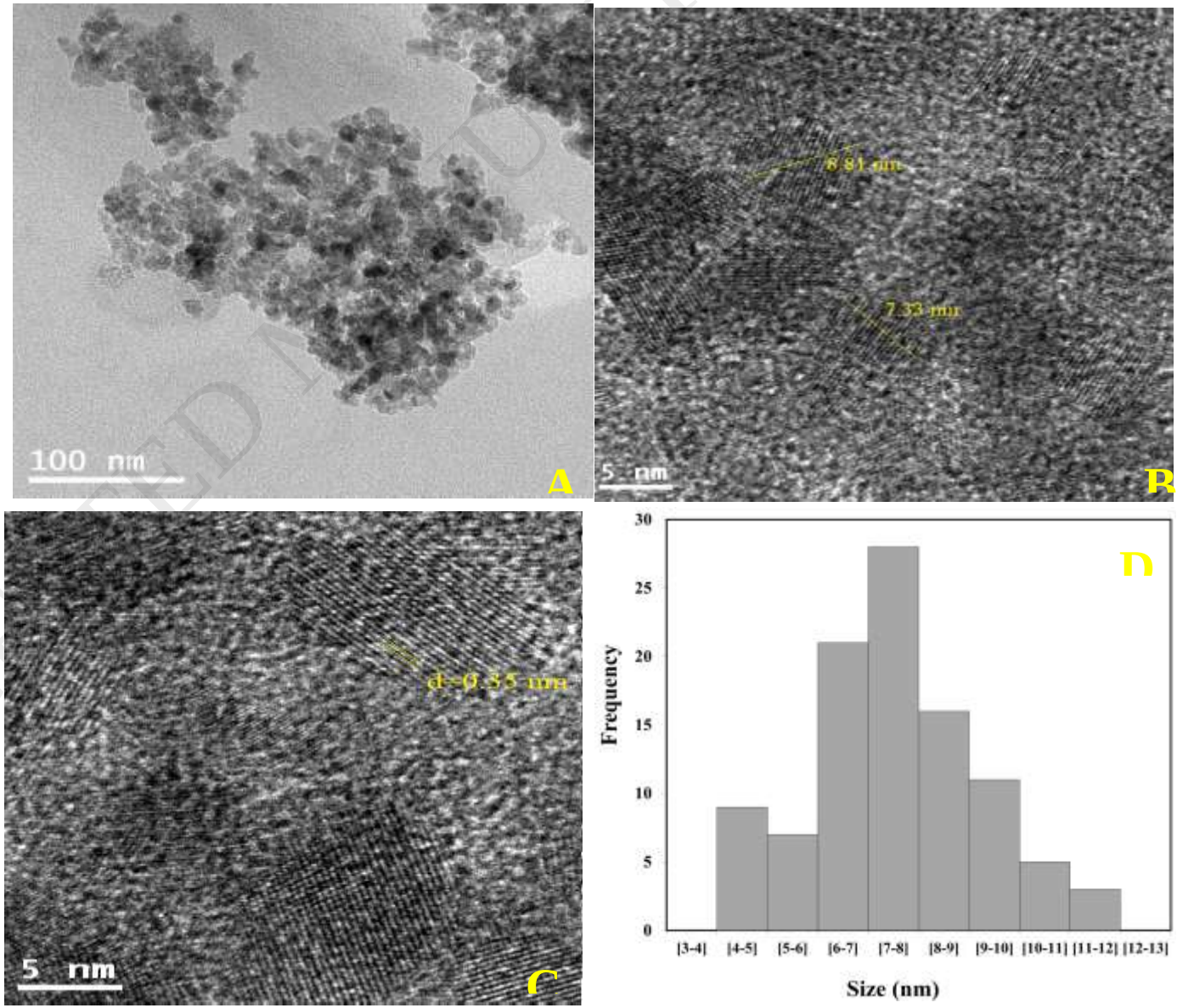

Fig. 6. TEM (a) and HRTEM (b and c) images of H-Base. (d) Particle size distribution histogram of H-Base sample measured from the TEM imaging in Fig. 6a (the graph is based on the measurement of the size of 100 nanoparticles.)

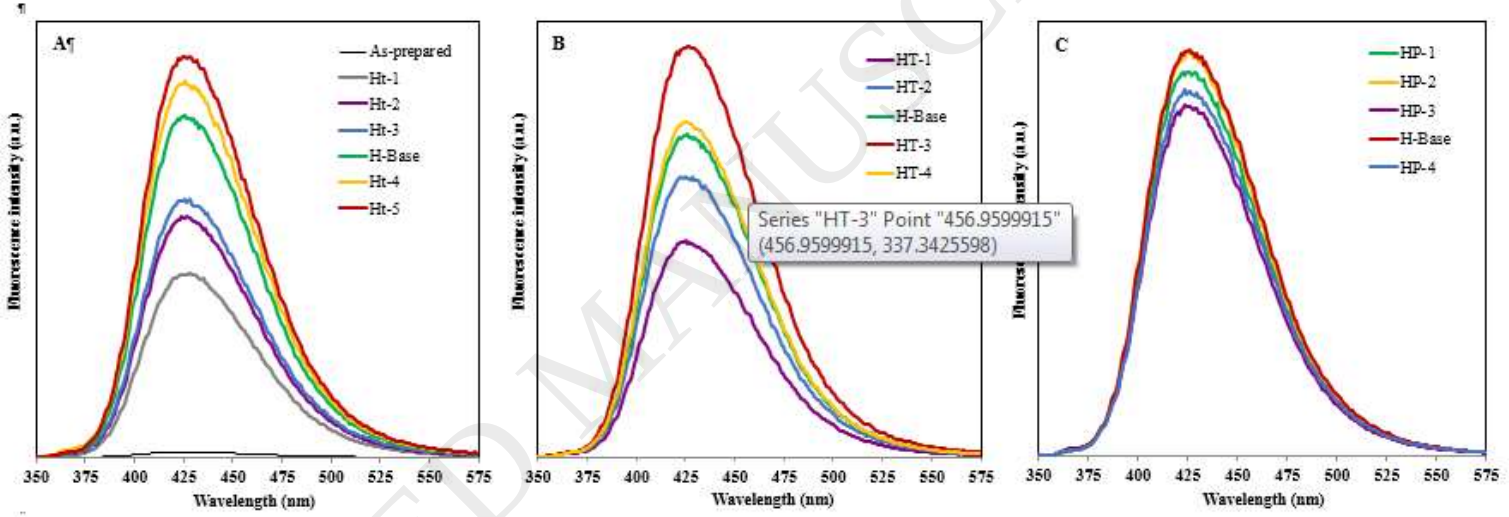

Fig. 7. Variations in Photoluminescence spectra of titania photocatalysts with (a) hydrothermal duration, (b) hydrothermal temperature, and (c) autoclave filling ratio.

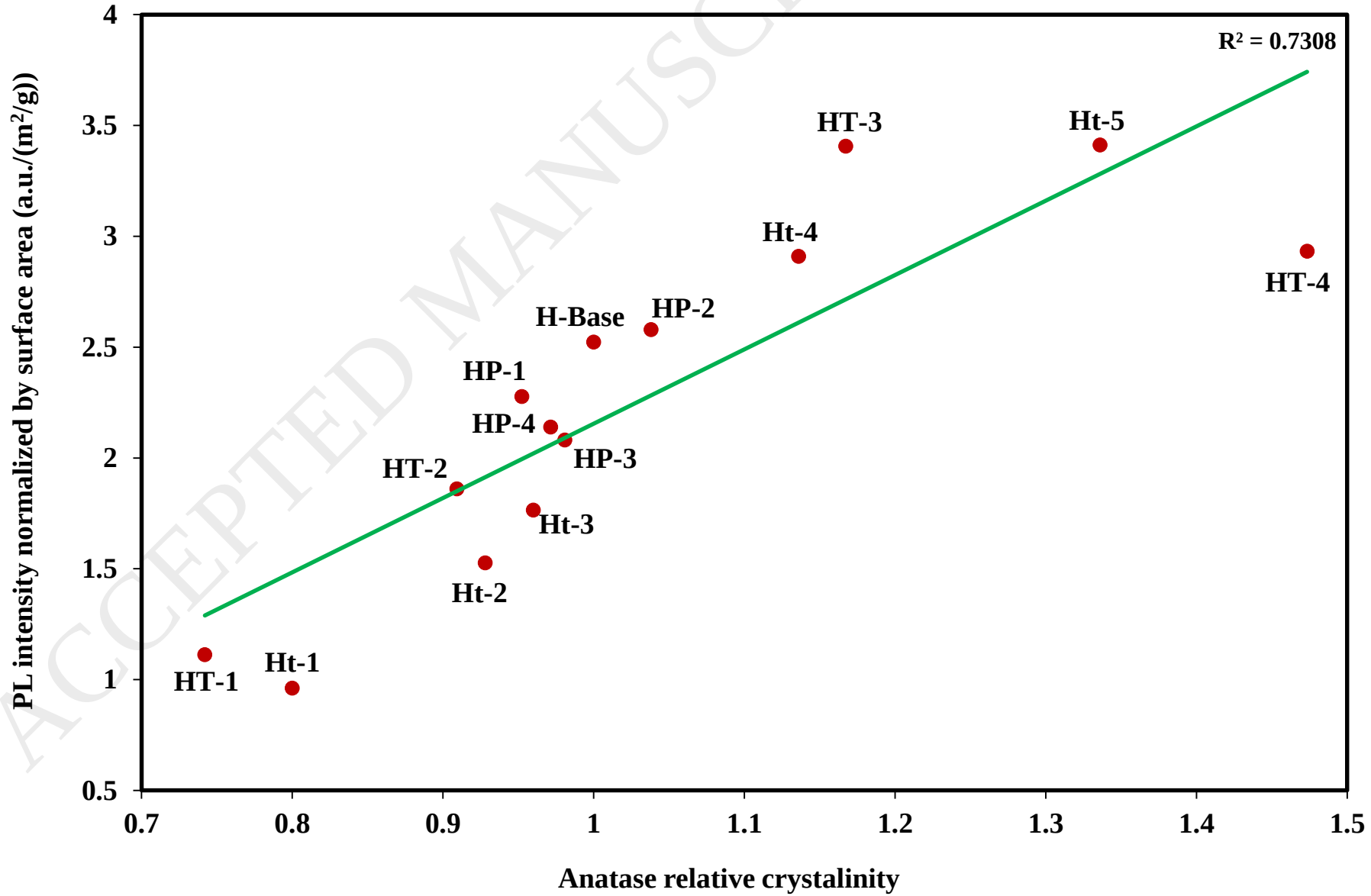

Fig. 8. Dependence of surface area normalized fluorescence intensity (a.u./(m^2/g)) on the relative anatase crystallinity of various titania photocatalysts (see Table 2).

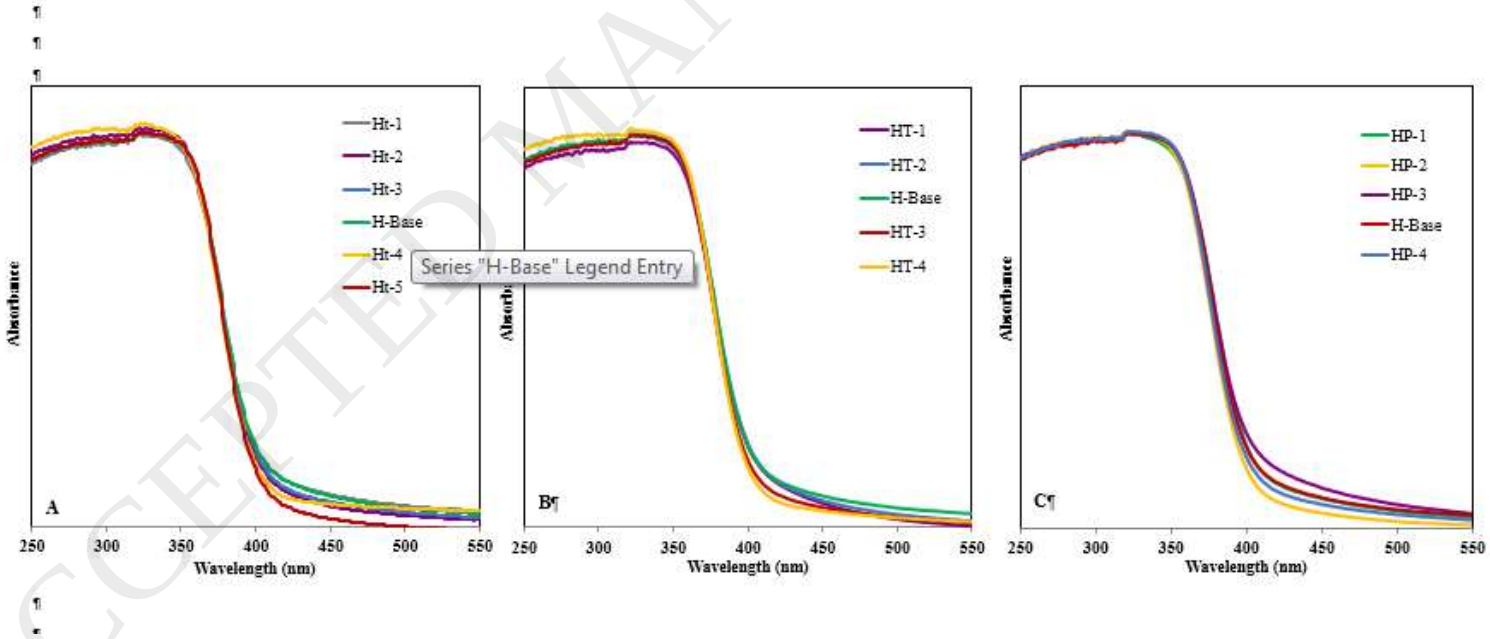

Fig. 9. Variations in UV-vis absorbance spectra of titania photocatalysts with (a) hydrothermal duration, (b) hydrothermal temperature, and (c) autoclave filling ratio.

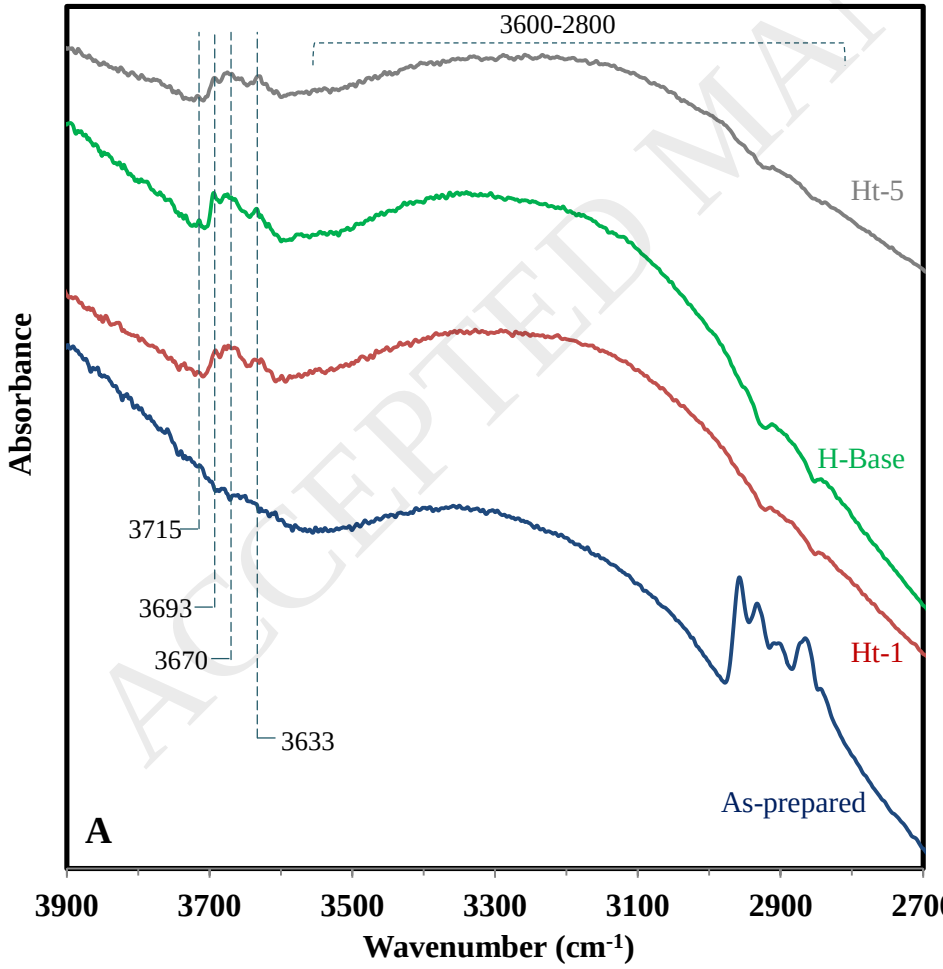

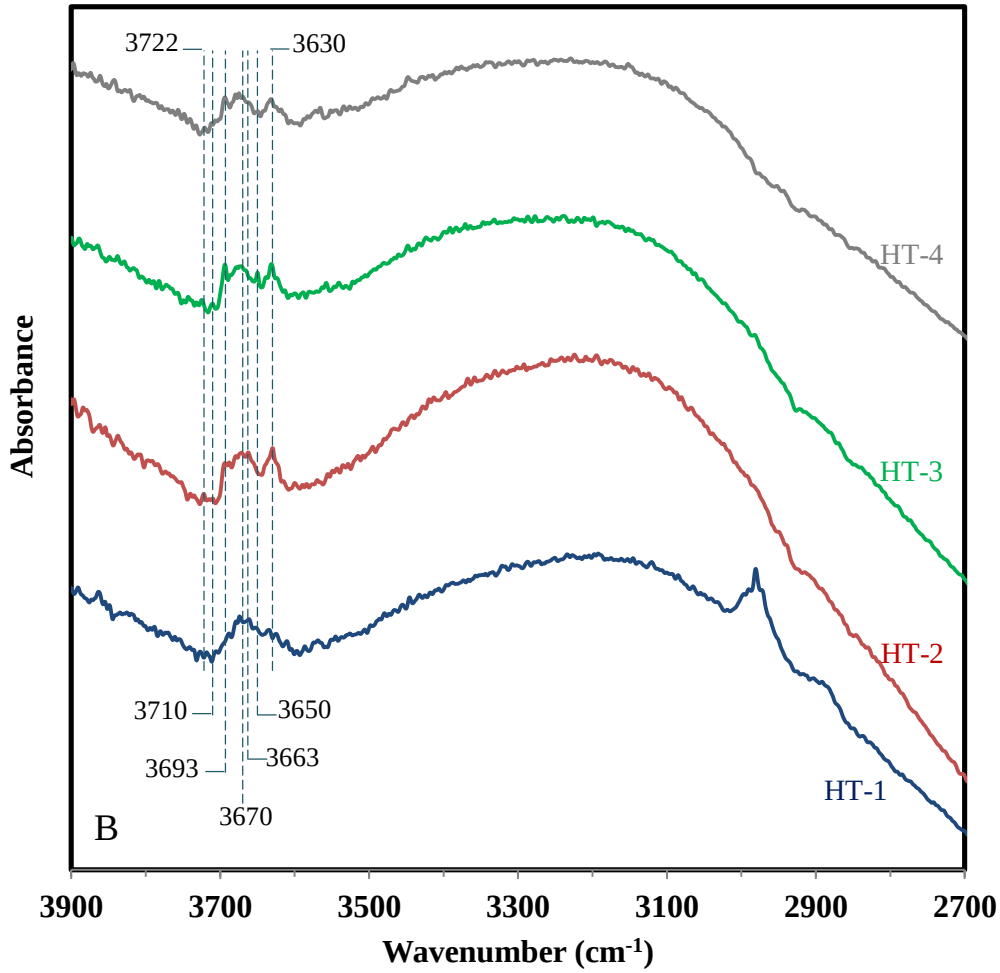

Fig. 10. FTIR spectra of the TiO_2 samples in the hydroxyl group region: (a) impact of hydrothermal time and (b) impact of hydrothermal temperature.

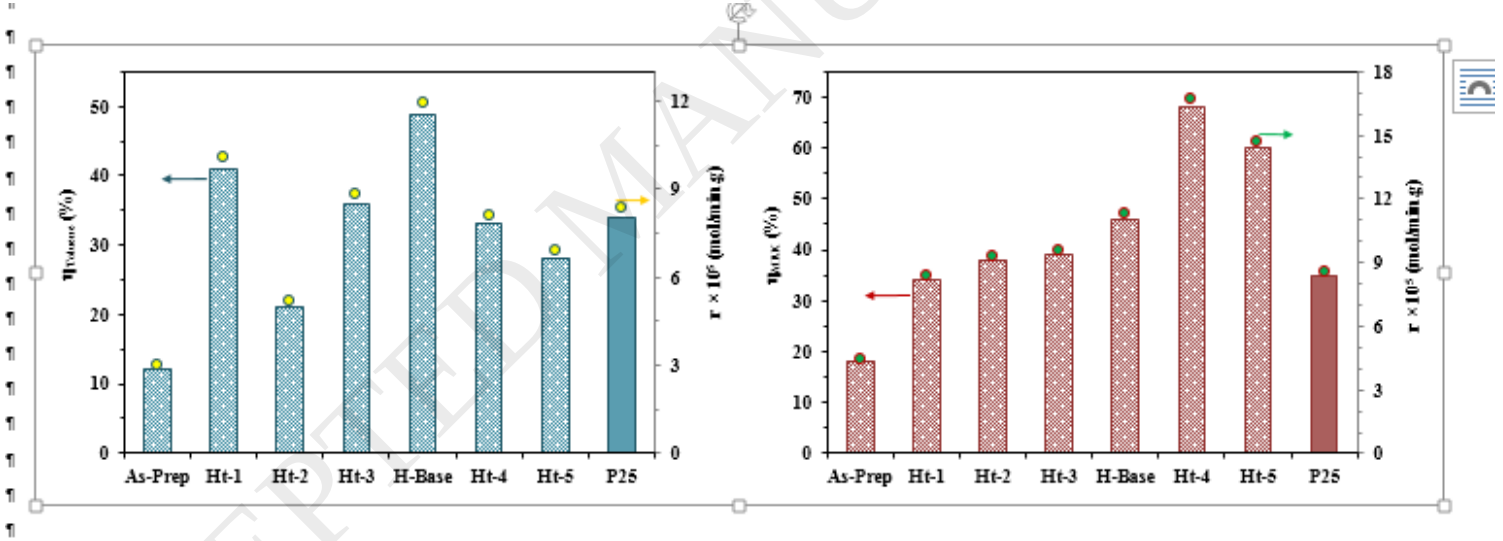

Fig. 11. Toluene and MEK removal efficiency and reaction rate for the as-prepared titania, hydrothermally-prepared TiO_2 samples synthesized at different durations (1-48 h), and P25.

Fig. 11. Toluene and MEK removal efficiency and reaction rate for the as-prepared titania, hydrothermally-prepared TiO_2 samples synthesized at different durations (1-48 h), and P25.

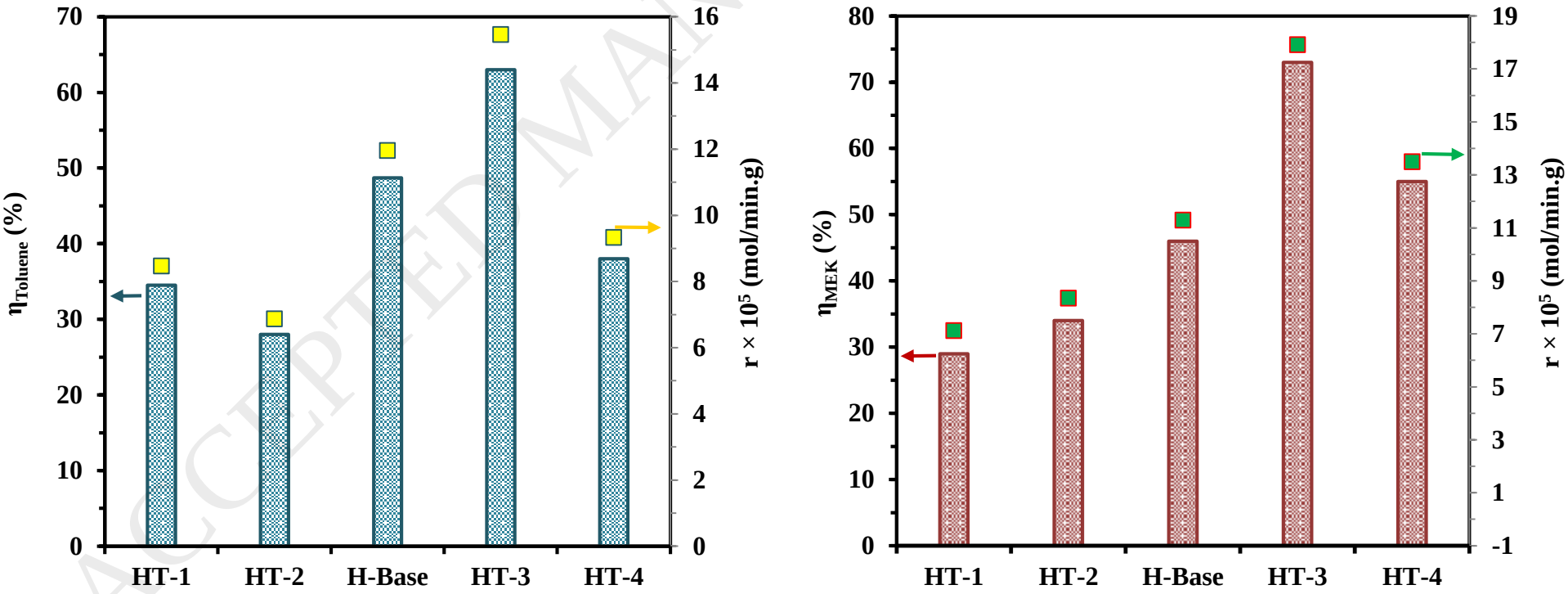

Fig. 12. Toluene and MEK removal efficiency and reaction rate for hydrothermally-prepared TiO_2 samples synthesized at different hydrothermal temperatures (100-220 °C).

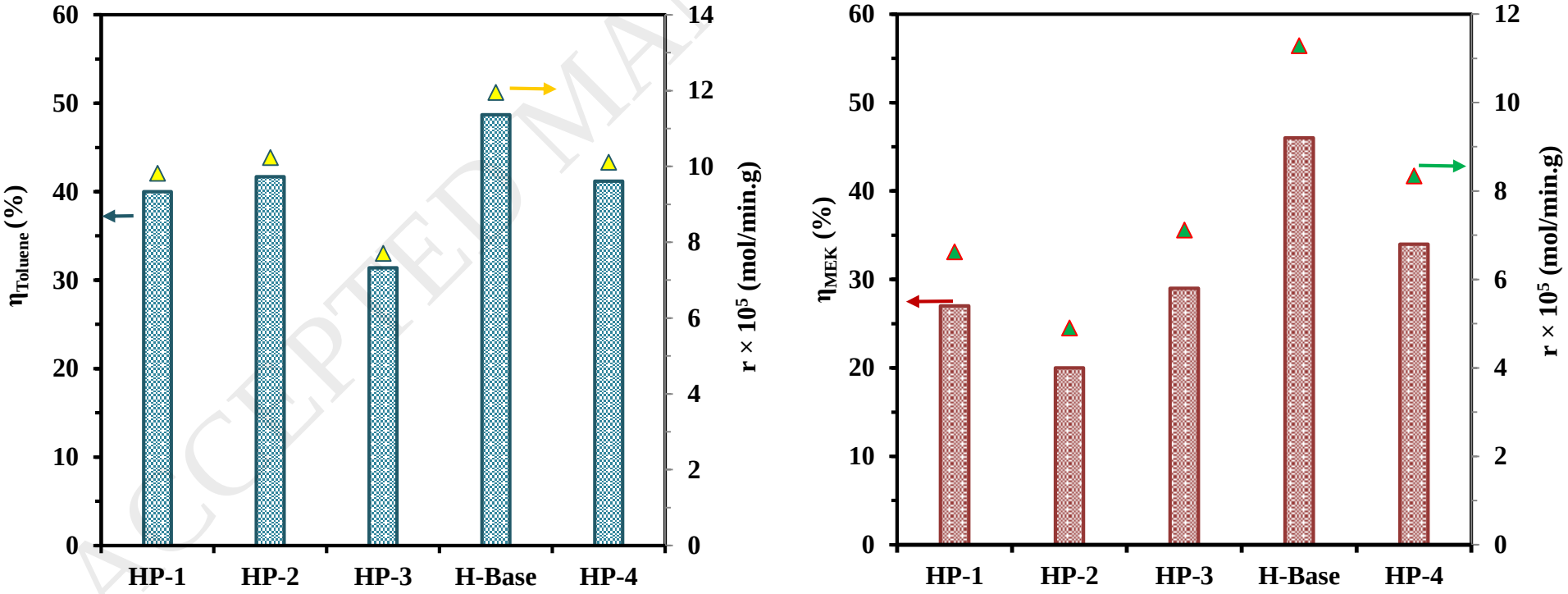

Fig. 13. Toluene and MEK removal efficiency and reaction rate for hydrothermally-prepared TiO_2 samples synthesized at different autoclave filling ratios (20-90%).

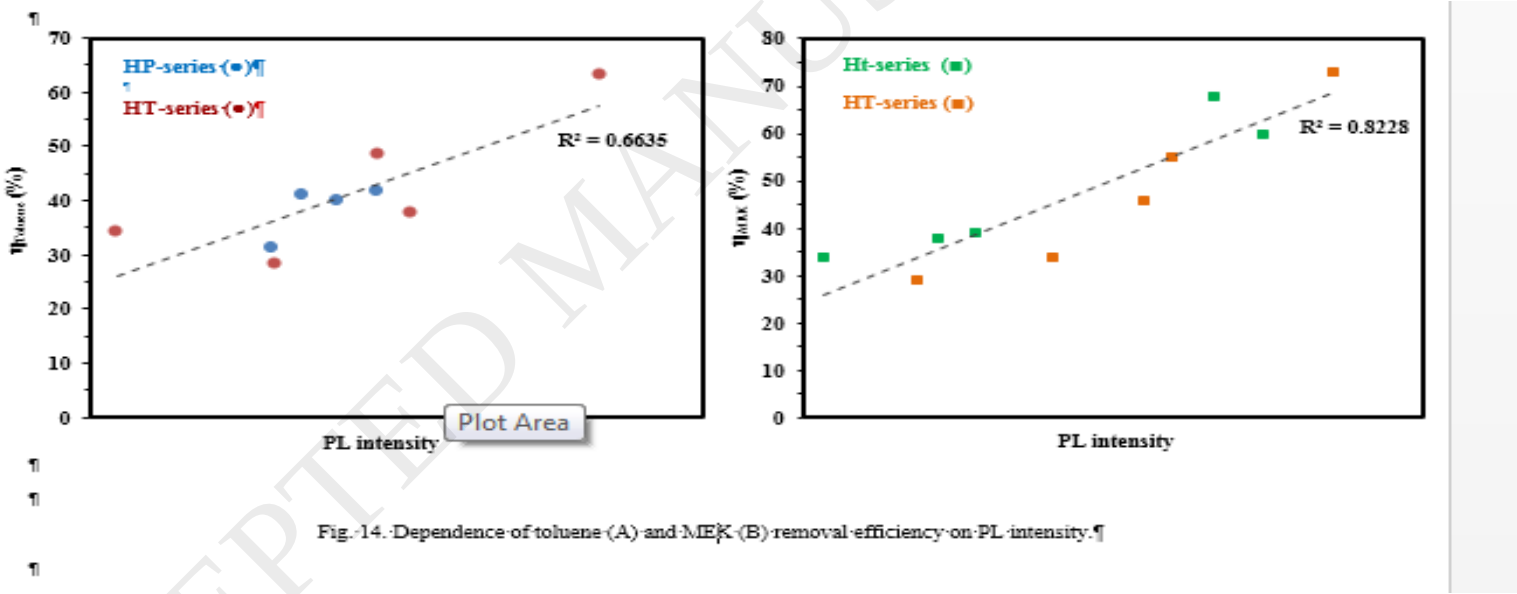

Fig. 14. Dependence of toluene (A) and MEK (B) removal efficiency on PL intensity.

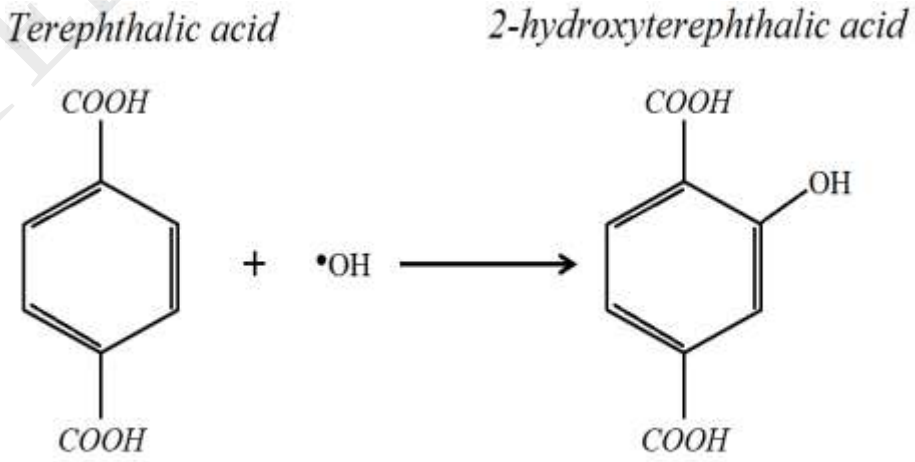

Scheme 1. Generation of 2-hydroxyterephthalic acid as a result of the reaction between terephthalic acid and hydroxyl radical.

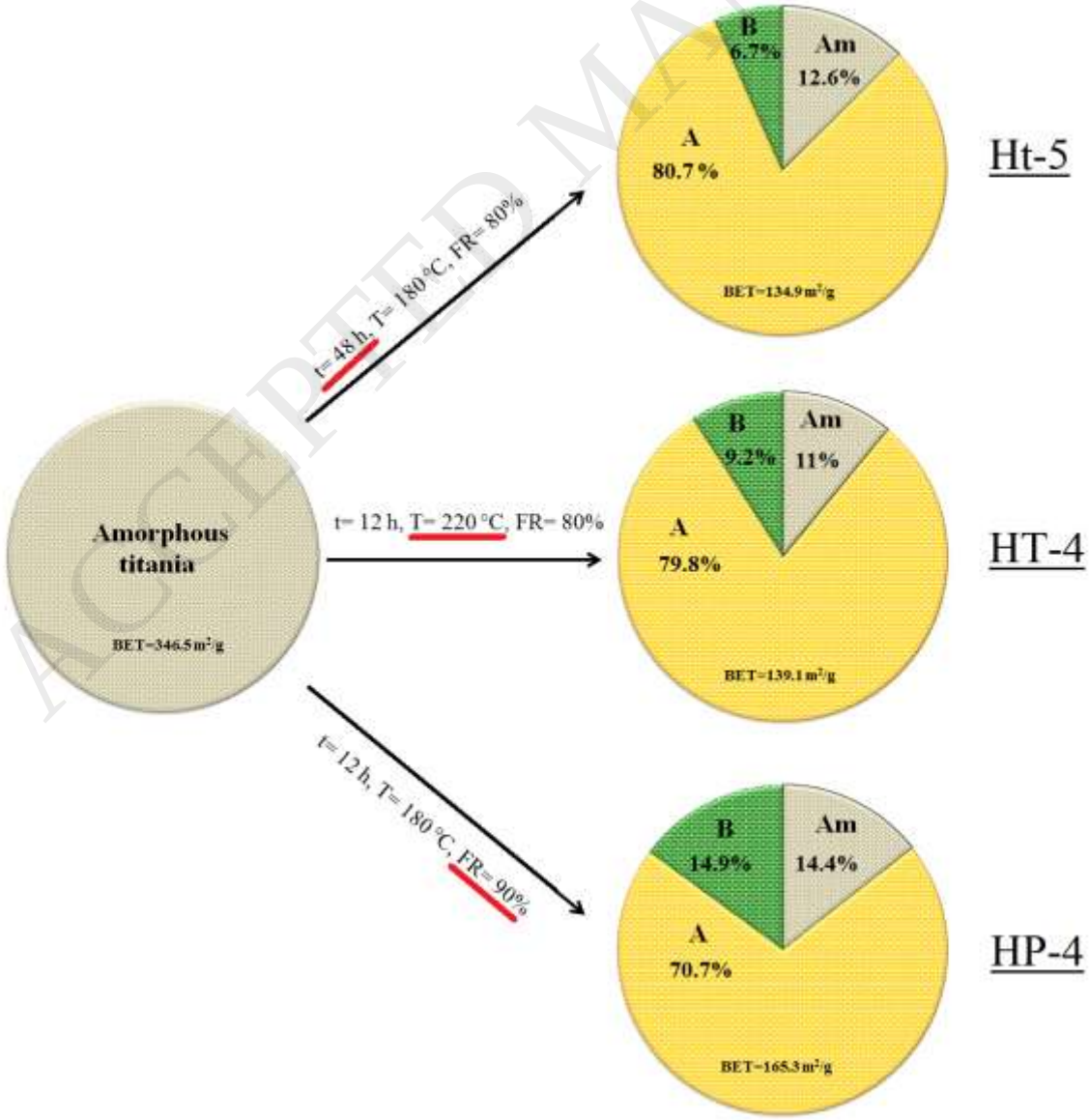

Scheme 2. Graphical presentation of the impact of hydrothermal treatment on titania structure.

Table 1. Hydrothermal preparation conditions of different TiO_2 photocatalysts.

Name*	Preparation parameters		
	Temperature (˚C)	Time (h)	Filling percentage (%)
H-Base	180	12	80
Ht-1	180	1	80
Ht-2	180	3	80
Ht-3	180	6	80
Ht-4	180	24	80
Ht-5	180	48	80
HT-1	100	12	80
HT-2	140	12	80
HT-3	200	12	80
HT-4	220	12	80
HP-1	180	12	20
HP-2	180	12	40
HP-3	180	12	60
HP-4	180	12	90

*In naming, t, T, and P respectively stand for time, temperature and pressure of hydrothermal reactions.

Table 2. PCO tests experimental conditions (mean value ± standard deviation)

Parameter	Value	Unit
Inlet concentration	1010 ± 51.3	ppb
Relative humidity	19.9 ± 2.0	%
Volumetric flow rate	12 ± 0.1	L/min
Residence time	0.05 ± 0.0004	Sec
Light intensity	5	mW/cm^2
Temperature	23.3 ± 1.4	°C
TiO_2 concentration	1± 0.07	mg/cm^2

Table 3. Crystalline and textural properties of titania photocatalysts prepared at various hydrothermal conditions and P25.

Name	Amorphous content (%)	Crystalline phase (%)		Crystal size (nm)		Relative anatase crystallinity	Surface area (m^2/g)	Band gap (eV)
		A	B	A	B			
P25	9.0	81.3	18.7 (R)	25.3	27.4 (R)	-	53.23	3.01
As-prepared	100	-	-	-	-	-	346.5	-
H-Base	14.6	83.4	16.6	7.6	8.3	1	155.5	3.20
Ht-1	17.4	84.6	15.4	6.1	7.4	0.80	219.1	3.19
Ht-2	16.0	82.8	17.2	6.9	7.7	0.93	181.0	3.21
Ht-3	14.6	81.5	18.5	7.3	8.0	0.96	168.4	3.19
Ht-4	14.7	89.0	11.0	7.9	8.5	1.14	148.3	3.21
Ht-5	12.6	92.3	7.7	8.8	9.2	1.34	134.9	3.21
HT-1	20.5	82.3	17.7	5.9	7.3	0.74	237.2	3.20
HT-2	15.9	83.1	16.9	6.9	7.9	0.90	183.5	3.19

HT-3	12.3	82.3	17.7	8.4	8.7	1.16	146.7	3.21
HT-4	11.0	89.7	10.3	9.5	10.0	1.47	139.1	3.22
HP-1	15.1	83.7	16.3	7.2	8.3	0.95	163.2	3.18
HP-2	14.5	83.2	16.8	8.4	8.9	1.04	151.4	3.22
HP-3	14.4	82.8	17.2	7.8	8.4	0.98	162.7	3.19
HP-4	14.4	81.5	18.5	7.7	8.7	0.97	165.3	3.21

* Relative anatase crystalinity is calculated by divinding the intensity of the anatase (101) diffraction peak to that of H-Base. A: anatase, B: brookite, R: rutile

Table 4. Generated by-products in the gas phase during photocatalytic degradation of toluene and MEK on various titania photocatalysts (all values in ppb).

Photocatalyst	**Toluene**			**MEK**			
	Formaldehyde	Acetaldehyde	Acetone	Formaldehyde	Acetaldehyde	Acetone	Propionaldehyde
P25	14.7	3.4	3.4	46.3	60.4	8.5	-
As-prepared	20.8	6.0	5.9	17.5	9.4	-	6.0
H-Base	13.0	4.6	-	43.9	45.6	-	-
Ht-1	13.2	4.6	6.5	33.3	31.7	-	-
Ht-2	11.3	3.9	5.7	35.8	34.4	-	6.1
Ht-3	13.7	5.3	6.4	36.6	34.4	6.7	4.6
Ht-4	12.5	4.4	5.1	38.2	37.2	-	-
Ht-5	12.6	5.0	6.2	40.0	36.5	10.8	5.3
HT-1	8.4	3.3	-	32.7	30.6	7.6	-
HT-2	10.7	4.5	6.1	38.2	35.6	7.8	-
HT-3	17.5	7.3	6.6	35.8	34.4	7.4	-
HT-4	16.2	5.8	5.8	34.6	33.0	7.1	-
HP-1	10.4	4.5	7.0	42.5	35.8	6.2	-
HP-2	10.8	4.5	10.5	40.0	33.0	-	-
HP-3	9.5	3.1	5.6	43.1	40.6	-	-
HP-4	9.9	5.3	8.4	37.4	36.7	-	-

Figure caption

Scheme 1. Generation of 2-hydroxyterephthalic acid as a result of the reaction between terephthalic acid and hydroxyl radical.

Scheme 2. Graphical presentation of the impact of hydrothermal treatment on titania structure.

Fig. 1. Schematic presentation of the experimental set-up for PCO experiments.

Fig. 2. XRD patterns of photocatalysts prepared at different (a) hydrothermal durations, (b) hydrothermal temperatures, and (c) autoclave filling ratios.

Fig. 3. Nitrogen adsorption–desorption isotherms of hydrothermally-prepared titania photocatalysts; Impact of hydrothermal preparation time (a) and temperature (b).

Fig. 4. Pore-size distribution of hydrothermally-prepared titania photocatalysts; Impact of hydrothermal preparation time (a) and temperature (b).

Fig. 5. (a and b) SEM images of porous TiO_2 hydrothermally prepared at 180 °C and 80% filling ratio for 12 h (H-Base). (c and d) SEM images of H-Base photocatalyst coated on nickel form filter.

Fig. 6. TEM (a) and HRTEM (b and c) images of H-Base. (d) Particle size distribution histogram of H-Base sample measured from the TEM imaging in Fig. 6a (the graph is based on the measurement of the size of 100 nanoparticles.)

Fig. 7. Variations in Photoluminescence spectra of titania photocatalysts with (a) hydrothermal duration, (b) hydrothermal temperature, and (c) autoclave filling ratio.

Fig. 8. Dependence of surface area normalized fluorescence intensity (a.u./(m^2/g)) on the relative anatase crystallinity of various titania photocatalysts (see Table 2).

Fig. 9. Variations in UV-vis absorbance spectra of titania photocatalysts with (a) hydrothermal duration, (b) hydrothermal temperature, and (c) autoclave filling ratio.
Fig. 10. FTIR spectra of the TiO_2 samples in the hydroxyl group region: (a) impact of hydrothermal time and (b) impact of hydrothermal temperature.

Fig. 11. Toluene and MEK removal efficiency and reaction rate for the as-prepared titania, hydrothermally-prepared TiO_2 samples synthesized at different durations (1-48 h), and P25.

Fig. 12. Toluene and MEK removal efficiency and reaction rate for hydrothermally-prepared TiO_2 samples synthesized at different hydrothermal temperatures (100-220 °C).

Fig. 13. Toluene and MEK removal efficiency and reaction rate for hydrothermally-prepared TiO_2 samples synthesized at different autoclave filling ratios (20-90%).

Fig. 14. Dependence of toluene (A) and MEK (B) removal efficiency on PL intensity.